

Escherichia coli-Specific CXCL13-Producing T_{FH} Are Associated with Clinical Efficacy of Neoadjuvant PD-1 Blockade against Muscle-Invasive Bladder Cancer



Anne-Gaëlle Goubet^{1,2,3}, Leonardo Lordello^{1,3}, Carolina Alves Costa Silva^{1,2,3,4}, Isabelle Peguillet^{1,3}, Marianne Gazzano^{1,3,5}, Maxime Descartes Mbognign-Fonkou^{1,3}, Cassandra Thelemaque^{1,3}, Cédric Lebacle⁶, Constance Thibault⁷, François Audenet⁸, Géraldine Pignot⁹, Gwenaelle Gravis¹⁰, Carole Helissey¹¹, Luca Campedel¹², Morgan Roupert¹³, Evangelos Xylinas¹⁴, Idir Ouzaid¹⁴, Agathe Dubuisson^{1,3}, Marine Mazzenga^{1,3}, Caroline Flament^{1,3}, Pierre Ly^{1,3}, Virginie Marty^{1,15}, Nicolas Signolle^{1,15}, Allan Sauvat^{1,16,17}, Thomas Sbarrato¹⁸, Mounia Filahi¹⁸, Caroline Davin¹⁸, Gabriel Haddad¹⁹, Jacques Bou Khalil¹⁹, Camille Bleriot^{1,3}, François-Xavier Danlos^{1,2,3}, Garrett Dunsmore^{1,2,3}, Kevin Mulder^{1,2,3}, Aymeric Silvin^{1,3}, Thibault Raoult^{1,20}, Baptiste Archambaud^{1,21}, Shaima Belhechmi^{1,21}, Ivo Gomperts Boneca²², Nadège Cayet²³, Maryse Moya-Nilges²³, Adeline Mallet²³, Romain Daillyere²⁴, Etienne Rouleau²⁵, Camelia Radulescu²⁶, Yves Allory²⁶, Jacques Fieschi¹⁸, Mathieu Rouanne^{1,2,3,27}, Florent Ginhoux^{1,2,28,29}, Gwénaël Le Teuff^{1,21}, Lisa Derosa^{1,2,3}, Aurélien Marabelle^{1,2,3,4,30}, Jeroen Van Dorp³¹, Nick Van Dijk³², Michiel S. Van Der Heijden^{31,32}, Benjamin Besse^{1,2,30,33}, Fabrice Andre^{1,2,30,33,34}, Miriam Merad^{35,36,37,38,39}, Guido Kroemer^{1,16,17,40}, Jean-Yves Scoazec^{1,2,15,41}, Laurence Zitvogel^{1,2,3,4}, and Yohann Loriot^{1,2,30,33,34,42}

ABSTRACT

Biomarkers guiding the neoadjuvant use of immune-checkpoint blockers (ICB) are needed for patients with localized muscle-invasive bladder cancers (MIBC). Profiling tumor and blood samples, we found that follicular helper CD4⁺ T cells (T_{FH}) are among the best therapeutic targets of pembrolizumab correlating with progression-free survival. T_{FH} were associated with tumoral CD8 and PD-L1 expression at baseline and the induction of tertiary lymphoid structures after pembrolizumab. Blood central memory T_{FH} accumulated in tumors where they produce CXCL13, a chemokine found in the plasma of responders only. IgG4⁺CD38⁺ T_{FH} residing in bladder tissues correlated with clinical benefit. Finally, T_{FH} and IgG directed against urothelium-invasive *Escherichia coli* dictated clinical responses to pembrolizumab in three independent cohorts. The links between tumor infection and success of ICB immunomodulation should be prospectively assessed at a larger scale.

SIGNIFICANCE: In patients with bladder cancer treated with neoadjuvant pembrolizumab, *E. coli*-specific CXCL13 producing T_{FH} and IgG constitute biomarkers that predict clinical benefit. Beyond its role as a biomarker, such immune responses against *E. coli* might be harnessed for future therapeutic strategies.

INTRODUCTION

Programmed cell death protein 1 (PD-1) is an immune-checkpoint protein expressed on T cells (1). PD-1 inhibits T-cell responses to cancer after binding to one of its ligands, programmed cell death ligand 1 (PD-L1, B7-H1, CD274) or PD-L2 (B7-DC, CD273; refs. 2, 3). Therapeutic

blockade of PD-1 or PD-L1 with monoclonal antibodies (mAb) leads to durable tumor regression in patients with several cancer types (1, 4–6). These clinical observations have spurred the FDA approval of two anti-PD-1 antibodies, pembrolizumab (MK-3475) and nivolumab (BMS-936558), for the treatment of localized and metastatic cancers across numerous indications.

¹Gustave Roussy, Villejuif, France. ²Faculté de Médecine, Université Paris-Saclay, Kremlin-Bicêtre, France. ³Institut National de la Santé Et de la Recherche Médicale (INSERM) U1015, Equipe Labelisée—Ligue Nationale contre le Cancer, Villejuif, France. ⁴Center of Clinical Investigations for In Situ Biotherapies of Cancer (BIOTHERIS), INSERM CIC1428, Villejuif, France. ⁵Sorbonne Université, Inserm, Centre d'Immunologie et des Maladies Infectieuses (CIMI-Paris), Département d'Immunologie, Assistance Publique Hôpitaux de Paris (AP-HP), Hôpital Pitié-Salpêtrière, Paris, France. ⁶Urology Department, University Hospital of Bicêtre-Paris Sud-Saclay University, Le Kremlin Bicêtre, Paris, France. ⁷Oncology Department, Hôpital Européen Georges Pompidou, AP-HP, University of Paris, Paris, France. ⁸Department of Urology, Hôpital Européen Georges Pompidou, AP-HP Centre, Université de Paris, Paris, France. ⁹Department of Surgical Oncology 2, Institut Paoli-Calmettes Cancer Center, Marseille, France. ¹⁰Department of Medical Oncology, Institut Paoli-Calmettes, Aix-Marseille University, CRCM, Marseille, France. ¹¹Military Hospital Begin, Saint-Mandé, France. ¹²Sorbonne Université, AP-HP, Hôpital de La Pitié-Salpêtrière, Institut Universitaire de Cancérologie, Département d'Oncologie Médicale, CLIP2 Galilée, Paris, France. ¹³GRC 5 Predictive Onco-Uro, Sorbonne University, Department of Urology, AP-HP, Pitie-Salpetrière Hospital, Paris, France. ¹⁴Department of Urology, Bichat-Claude Bernard Hospital, Paris University, Paris France. ¹⁵Experimental and Translational Pathology Platform (PETRA), AMMICa, INSERM US23/UAR3655, Gustave Roussy, Villejuif, France. ¹⁶Equipe 11 Labelisée par la Ligue Nationale contre le Cancer, Centre de Recherche des Cordeliers, Institut National de la Santé et de la Recherche Médicale U1138, Université de Paris, Sorbonne Université, Paris, France. ¹⁷Metabolomics and Cell Biology Platforms, Gustave Roussy, Villejuif, France. ¹⁸Veracyte, Marseille, France. ¹⁹Aix-Marseille University, IRD, APHM, MEPHI, Institut Hospitalo-Universitaire Méditerranée Infection, Marseille, France. ²⁰Service de Promotion des Etudes Cliniques (SPEC), Gustave Roussy, Université Paris-Saclay, Villejuif, France. ²¹Service de Biostatistiques et d'Epidémiologie, Gustave Roussy, Villejuif, France. ²²Institut Pasteur, Université de Paris, CNRS UMR2001, INSERM U1306, Unité de Biologie et Génétique de la Paroi Bactérienne, Paris, France. ²³Core Facility Ultrastructural Biologimaging Core Facility, Institut Pasteur, Paris France. ²⁴EverImmune, Gustave Roussy, Villejuif, France. ²⁵Department of Medical Biology and Pathology, Cancer

Genetics Laboratory, Gustave Roussy, Villejuif, France. ²⁶Department of Pathology, Hôpital Foch, UVSQ-Université Paris-Saclay, Suresnes, France. ²⁷Department of Urology, Hôpital Foch, UVSQ-Université Paris-Saclay, Suresnes, France. ²⁸Singapore Immunology Network (SIgn), A*STAR, Singapore, Singapore. ²⁹Shanghai Institute of Immunology, Shanghai Jiao Tong University School of Medicine, Shanghai, China. ³⁰Cancer Medicine Department, Gustave Roussy, Villejuif, France. ³¹Department of Molecular Carcinogenesis, Netherlands Cancer Institute, Amsterdam, the Netherlands. ³²Department of Medical Oncology, Netherlands Cancer Institute, Amsterdam, the Netherlands. ³³INSERM U981, Biomarqueurs Prédictifs et Nouvelles Stratégies Thérapeutiques en Oncologie, Villejuif, France. ³⁴PRISM Precision Cancer Center, Gustave Roussy, Villejuif, France. ³⁵The Precision Immunology Institute, Icahn School of Medicine at Mount Sinai, New York, New York. ³⁶Human Immune Monitoring Center, Icahn School of Medicine at Mount Sinai, New York, New York. ³⁷The Tisch Cancer Institute, Icahn School of Medicine at Mount Sinai, New York, New York. ³⁸Department of Oncological Sciences, Icahn School of Medicine at Mount Sinai, New York, New York. ³⁹Institute for Thoracic Oncology, Icahn School of Medicine at Mount Sinai, New York, New York. ⁴⁰Pôle de Biologie, Hôpital Européen Georges Pompidou, AP-HP, Paris, France. ⁴¹Department of Medical Biology and Pathology, Gustave Roussy, Villejuif, France. ⁴²Early Drug Development Department (DITEP), Gustave Roussy, Villejuif, France.

Note: L. Lordello and C. Alves Costa Silva contributed equally to this article. L. Zitvogel and Y. Loriot are the co-last authors of this article.

Current address for M. Rouanne: Department of Microbiology and Immunology, Vagelos College of Physicians and Surgeons, Columbia University, New York, New York.

Corresponding Author: Laurence Zitvogel, Clinicobiome, Institut Gustave Roussy, 114 rue Edouard Vaillant, Villejuif 94805, France. Phone: 331-4211-5041; Fax: 331-4211-6094; E-mail: Laurence.zitvogel@gustaveroussy.fr
Cancer Discov 2022;12:2280–307

doi: 10.1158/2159-8290.CD-22-0201

©2022 American Association for Cancer Research

Pembrolizumab targets epitopes on the PD-1 molecule with high affinity and specificity. This mAb is of the IgG4 subclass and hence has low affinity for C1q and Fc receptors (7). Pharmacokinetic studies based on flow-cytometric methods (8) indicated a dose-independent high receptor occupancy at the peak and a plateau reached at 60 days (8). Preclinical studies in immunodeficient NOD/SCID/ γ_c^{null} mice transplanted with human CD34⁺ hematopoietic stem cells and inoculated with partially histocompatible patient-derived xenografts unveiled that pembrolizumab stimulated anticancer T-cell responses (9). Following PD-1 blockade, both CD4⁺ and CD8⁺ T cells expanded in blood, but CD8⁺ T cells were mandatory for the antitumor efficacy of pembrolizumab and migrated from tumor margins to nests (9). In patients, pembrolizumab promotes minor changes in blood while mobilizing not only T cells but also B cells and suppressive monocytes in tumors (10). However, expansion of effector memory CD8⁺ tumor-infiltrating lymphocytes (TIL) has been recognized as the best pharmacodynamic hallmark of bioactivity of these therapeutic mAbs against melanoma (10).

Urothelial carcinoma (UC) is a highly prevalent malignancy that remains difficult to treat in the case of muscle-invasive tumors (11). Nonmetastatic muscle-invasive bladder cancers (MIBC) are mainly treated with cisplatin-based neoadjuvant chemotherapy followed by radical cystectomy and harbor a poor prognosis, with a 5-year survival of 60% (12). However, a significant subset of patients are ineligible for neoadjuvant cisplatin-based chemotherapy. Since 2017, immune-checkpoint blockers (ICB), such as anti-PD-1/PD-L1 antibodies, have emerged as a successful immunotherapeutic strategy for advanced UC (13–18). Driven by the promising results in advanced diseases, ICB indications have been considered for the treatment of lower stage bladder tumors, including non-MIBC and nonmetastatic MIBC (NCT02844816, NCT02901548, and NCT02792192; refs. 19, 20). To our knowledge, four neoadjuvant trials investigating either anti-PD-1/PD-L1 monotherapy or the combination of anti-CTLA-4 and anti-PD-1/PD-L1 mAbs before cystectomy have been reported for cisplatin-ineligible patients or patients who declined neoadjuvant chemotherapy (21–24). Pathologic complete response (pCR), defined as the absence of tumor cells (ypT0N0; ref. 25), was observed in 31% to 46% of patients. Substantial toxicity (≥grade 3 immune-related adverse events) was reported in 11% and from 21% to 55% of patients treated with anti-PD-1/PD-L1 or combined ICB, respectively. Therefore, there is a need for biomarker discovery to increase the therapeutic index of neoadjuvant immunotherapy in MIBC.

In past trials revealing the efficacy of neoadjuvant ICBs in UC, immune or tumor expression of PD-L1 and tumor mutational burden (TMB) did not represent reliable baseline predictors of clinical benefit (21–24). In fact, responding tumors showed a predominant expression of genes related to tissue repair, whereas resistance was associated with stromal or cell-cycle fingerprints after neoadjuvant PD-L1 mAbs (23). This study also identified preexisting intraepithelial CD8⁺ T cells and a pro-Th1 signature as predictive biomarkers of pCR to PD-1/PD-L1 blockade. In accordance with previously described biomarkers in melanoma and sarcoma (26–28), tertiary lymphoid structures (TLS) represented the best predictors of clinical responses to neoadjuvant PD-1/PD-L1 plus

CTLA-4 blockade in high-grade MIBC (21, 24). Indeed, TLS identified by IHC were associated with a transcriptome blueprint centered around *CD79A*, *LAMP3*, *MS4A1*, and *POU2AF1* predicting pathologic responses (21). In parallel, mutation of *ARID1A* in tumor cells and expression of CXCL13 in tumor tissues at baseline may act as predictors of clinical response for patients receiving ICBs (29). However, these reports did not identify blood immune proxies associated with the local induction of TLS in the bladder (21, 24).

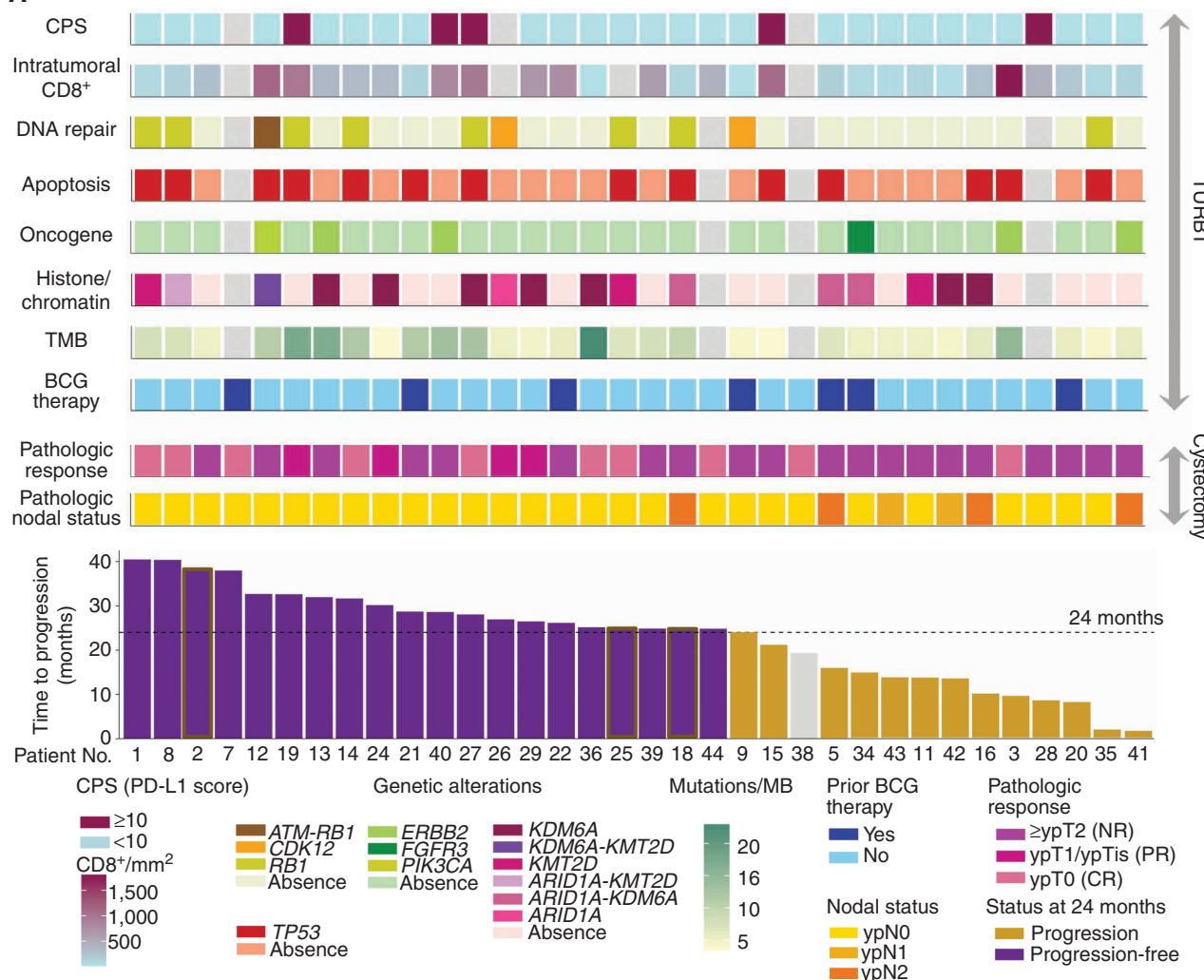
Follicular helper T cells (T_{FH}), a specialized subset of CD4⁺ effector T (TE) cells involved in germinal center reactions and affinity maturation of B cells, are known to orchestrate TLS formation. In a chronic viral infection, T_{FH} were shown to be mandatory to sustain virus-specific cytotoxic CD8⁺ T-cell (CTL) immune responses through IL21 production (30). During chronic inflammatory processes of carcinogenesis, the links between T_{FH} and CTL responses have only recently been discussed with the growing awareness of the clinical relevance of TLS (31, 32). For instance, in colon cancers, microbiota-specific T_{FH} responses were indispensable for TLS formation and tumor control in the absence of CTL effectors (33). In contrast, in rodent and human breast cancers, a functional T_{FH} response orchestrated in TILs within active TLS has been associated with cytotoxic CTL responses that governed their prognosis (34). Hence, by bridging the two arms of the adaptive immune system (B cells and CD8⁺ T cells) within TLS, T_{FH} indirectly contribute to exert an immune pressure against tumor progression in human and rodent ovarian cancers (35, 36).

When investigating the PANDORE single-arm, phase II trial (NCT03212651), which enrolled patients with MIBC treated with neoadjuvant pembrolizumab, we obtained evidence that T_{FH} stand among the main therapeutic targets of neoadjuvant pembrolizumab, both in blood and in the bladder. Baseline blood memory T_{FH} together with B cells became activated by pembrolizumab, facilitating the orchestration of tertiary lymphoid-like (TLS-like) structures and CD8⁺ TIL accumulation, translating into clinical benefit. Importantly, antibodies (IgG) and CXCL13 producing CD4⁺ T-cell memory responses against *Escherichia coli* (and not other urinary commensals) emerged as robust biomarkers of clinical benefit.

RESULTS

Clinical Efficacy of Pembrolizumab in the PANDORE Study

Between October 2017 and May 2019, we enrolled 44 cisplatin-ineligible patients with localized MIBC in the PANDORE trial (NCT03212651), but only 39 patients were included in the final analysis (Supplementary Fig. S1A and S1B). Among these patients, 25 (64%) met cisplatin ineligibility and 14 (36%) declined chemotherapy. Following baseline transurethral resection of bladder tumor (TURBT), 39 patients were then treated with pembrolizumab (200 mg) every 3 weeks for a total of three cycles before radical cystectomy (Supplementary Fig. S1B). Clinical and tumor characteristics are summarized in Supplementary Table S1 and Fig. 1. All tumors were UC. Briefly, most patients were men (74.4%), with a median age of 72 years [interquartile range (IQR): 67–78] and presented a clinical-stage cT2 (82.1%) and cN0 (89.7%). Nearly

A

Downloaded from http://aacjournals.org/cancerdiscovery/article-pdf/12/10/2280/3211219/2280.pdf by York University user on 21 January 2024

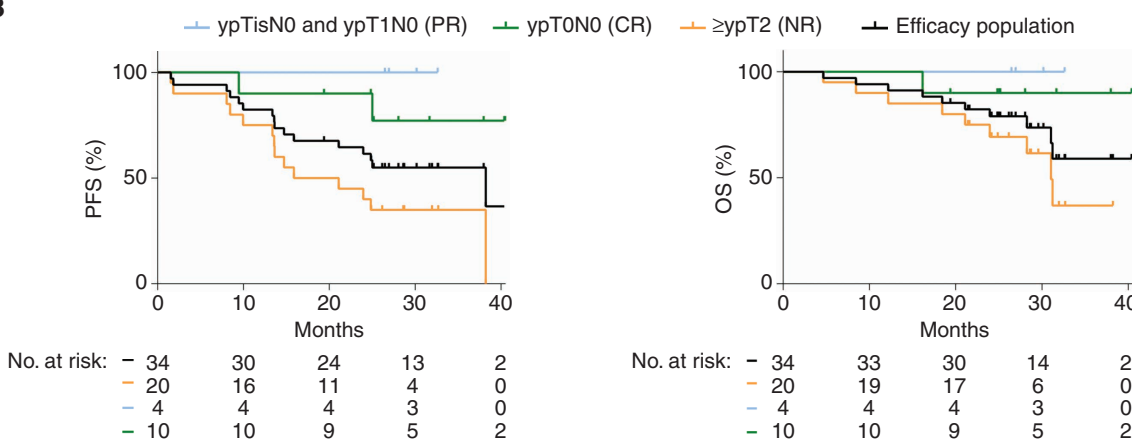
B

Figure 1. PANDORE patient characteristics and survival after neoadjuvant pembrolizumab. **A**, Clinical, biological, and pathologic characteristics of MIBC-bearing patients. Prior Bacillus Calmette-Guérin (BCG) therapy, PD-L1 combined positive score (CPS; clone: 22C3), intratumoral CD8 (CD8 clone, Veracity), TMB, and genetic alterations in oncogenes and tumor suppressor genes, in the apoptotic machinery, or in the DNA repair pathway are detailed for each individual, with a color code aligned at the bottom. Time to progression, with a dotted line for the cutoff value (24 months), used throughout the article is indicated. Missing values are shown in gray. CR, complete response; MB, megabase; NR, no response; PR, partial response. **B**, Kaplan-Meier survival curves for PFS (left) and OS (right) in the efficacy population (black) and according to the pathologic response (NR, orange; PR, light blue; and CR, green).

all patients ($n = 37/39$) received the planned three cycles of pembrolizumab. Patient #11 did not receive the last cycle due to grade 2 keratitis and patient #43 did not receive cycle 2 due to worsening adrenal insufficiency and fatigue. Sixty-two percent of individuals experienced a pembrolizumab-related adverse event, mostly grade 1 (Supplementary Table S2). No deaths related to therapy occurred. The median interval between the first infusion and radical cystectomy was 60 days (IQR: 55–63). Out of 39 patients, 34 proceeded with radical cystectomy (efficacy population; Supplementary Fig. S1A and S1C). The median time between the last cycle and radical cystectomy was 16 days (IQR: 13–21).

Radical cystectomy by open surgery was performed in 12 patients (35%). Postsurgical complications are detailed in Methods and were similar to those reported in other published studies (37, 38). The primary endpoint was pCR, defined as the absence of cancer cells in the bladder and the absence of microscopic lymph node metastases in the cystectomy specimen (ypT0N0). The overall pCR rate was 29.4% [95% confidence interval (CI): 15.1–47.5], and the overall downstaging [i.e., ypT0N0, ypTisN0, ypTaN0, and ypT1N0 and referred to as major pathologic response (MPR); ref. 25] was 41.2% (95% CI: 24.6–59.3; Fig. 1A).

The median follow-up in the efficacy population ($n = 34$) was 28.7 months (min: 19.4; max: 40.5) at data cutoff. A relapse or a death occurred in 16 patients (Fig. 1B; Supplementary Fig. S1C). The median progression-free survival (PFS) was 38.2 months (95% CI: 15.9–not reached; Fig. 1B, left). With 10 deaths among all 34 patients, overall survival (OS) was 94.1% at 1 year and 78.9% at 2 years. Median OS was not reached (95% CI: 31–not reached; Fig. 1B, right). Somatic DNA sequencing concerned the 450 genes of the Cancer Core Europe panel (39). The most recurrent causal variants are shown in Fig. 1A. The co-occurrence of causal variants *RB1* and *TP53* (observed in $n = 8/30$ MIBC) was associated with pCR and MPR ($P = 0.0042$ and $P = 0.031$, respectively, Fisher exact test) but not with PFS ($P = 0.16$, log-rank test). As reported earlier (22), high TMB was associated with prolonged PFS (Fig. 1A; Supplementary Fig. S2A).

Hence, the PANDORE study corroborated the efficacy of neoadjuvant ICBs in cisplatin-ineligible MIBC, as previously reported (21–24), with 29.4% and 60.6% of patients who exhibited a pCR and who did not relapse at 2 years after TURBT, respectively. The efficacy population ($n = 34$ patients; Supplementary Fig. S1A) was analyzed henceforth for biomarker discovery according to PFS with a cutoff value of 24 months ($n = 13$ with relapse and/or death occurring before 24 months and $n = 20$ censored at 24 months, excluding one patient whose follow-up did not reach 24 months), as most relapses occur within the first 24 months in trials investigating chemotherapy and ICB (19, 40).

Baseline T_{FH} Are Associated with Clinical Benefit to Neoadjuvant Pembrolizumab

To determine which immune parameter best predicts clinical benefit (MPR and PFS), we performed an exploratory biomarker analysis. We analyzed PD-L1 expression and TILs in tumors obtained through TURBT (pre-pembrolizumab) and on cystectomy (post-pembrolizumab; Supplementary Fig. S2B–S2F). First, we performed IHC staining using

anti-PD-L1, anti-CD3, and anti-CD8 antibodies in matched pre- and posttreatment specimens in 34 patients. PD-L1 expression was analyzed in immune and tumor cells using the combined positive score (CPS; clone: PD-L1 22C3; Fig. 1A; Supplementary Fig. S2B) on TURBT samples. Only five patients harbored a CPS ≥ 10 (16%), and CPS was associated with neither pCR ($P = 0.68$, χ^2 test) nor MPR ($P = 0.82$, χ^2 test). CPS failed to predict either PFS or OS (Supplementary Fig. S2B). Density and geodistribution of CD3⁺ and CD8⁺ cells, as well as clustering and proximity of PD-L1⁺ and CD8⁺ cells (Immunoscore IC), were evaluated (Fig. 2; Supplementary Fig. S2C and S2D). The density of CD8⁺ cells, pre- and post-pembrolizumab, was associated with PFS (Supplementary Fig. S2E and S2F, left). After PD-1 blockade, the proximity between CD8⁺ T and PD-L1⁺ cells was associated with prolonged PFS (Supplementary Fig. S2F, right). TLS-like were identified by microscopic morphology in hematoxylin-eosin-safran (HES)-stained tissues in association with CD20 and CD4, CD38, and PD-1 immunolabeling and classified as lymphoid aggregates (LA), resting follicles (RF), and germinal centers (GC). LA were determined as vaguely nodular aggregates of small noncleaved lymphoid cells, usually with more than 250 and fewer than 500 cells, without two or more of the early germinal center elements (follicular dendritic cells, centroblasts, mantle zone, or high endothelial veins); primary follicle-like TLS (RF) were determined as nodular aggregates of predominantly small lymphoid cells, usually with more than 500 cells, with three or more of the follicular elements, but without late germinal center elements (tinged body macrophages or dark/light areas of a clear germinal center, marginal zone); and secondary follicle-like TLS (GC) were determined as lymphoid follicles showing late germinal center structures.

Spearman correlation matrices establishing interconnections between all these pathologic factors are shown in Fig. 2A and B. Thus, the density of CD4⁺PD-1⁺ cells correlated with the density of CD8⁺ cells at baseline (Fig. 2A and B, left), and pembrolizumab triggered a coordinated association between the densities of TLS-like (and/or GC, RF, LA) and CD8⁺ cells (Fig. 2A and B, right). Moreover, the latter coincided with densities of CD4⁺PD-1⁺ ($P = 0.0022$ and $R = 0.66$, Spearman correlation) and anticorrelated with MPR ($P = 0.017$ and $R = -0.53$, Spearman correlation; Fig. 2A, right). Finally, although baseline density of TLS-like did not predict PFS ($P = 0.24$, log-rank test), pembrolizumab-induced TLS-like were associated with PFS ($P = 0.01$, log-rank test; Fig. 2C).

To investigate the coordination between tumoral TLS-like and CD8 infiltrates with blood immune profiles induced by PD-1 blockade, we performed cytometry by time-of-flight (CyTOF) on paired blood cells before, during, and after (cystectomy) three cycles of pembrolizumab in 38 patients. As mentioned above, the efficacy assessment was available for 34 of 38 patients. One hundred and fifty-three samples were barcoded (one barcode for one time point per patient) and stained with a 38-parameter antibody panel for high-dimensional characterization of the CD4 cell, CD8 cell, and B-cell heterogeneity based on canonical markers of polarization, differentiation, and activation/exhaustion (Supplementary Table S1; Supplementary Fig. S1A and S1B). Using the PhenoGraph algorithm, we analyzed the clinical significance

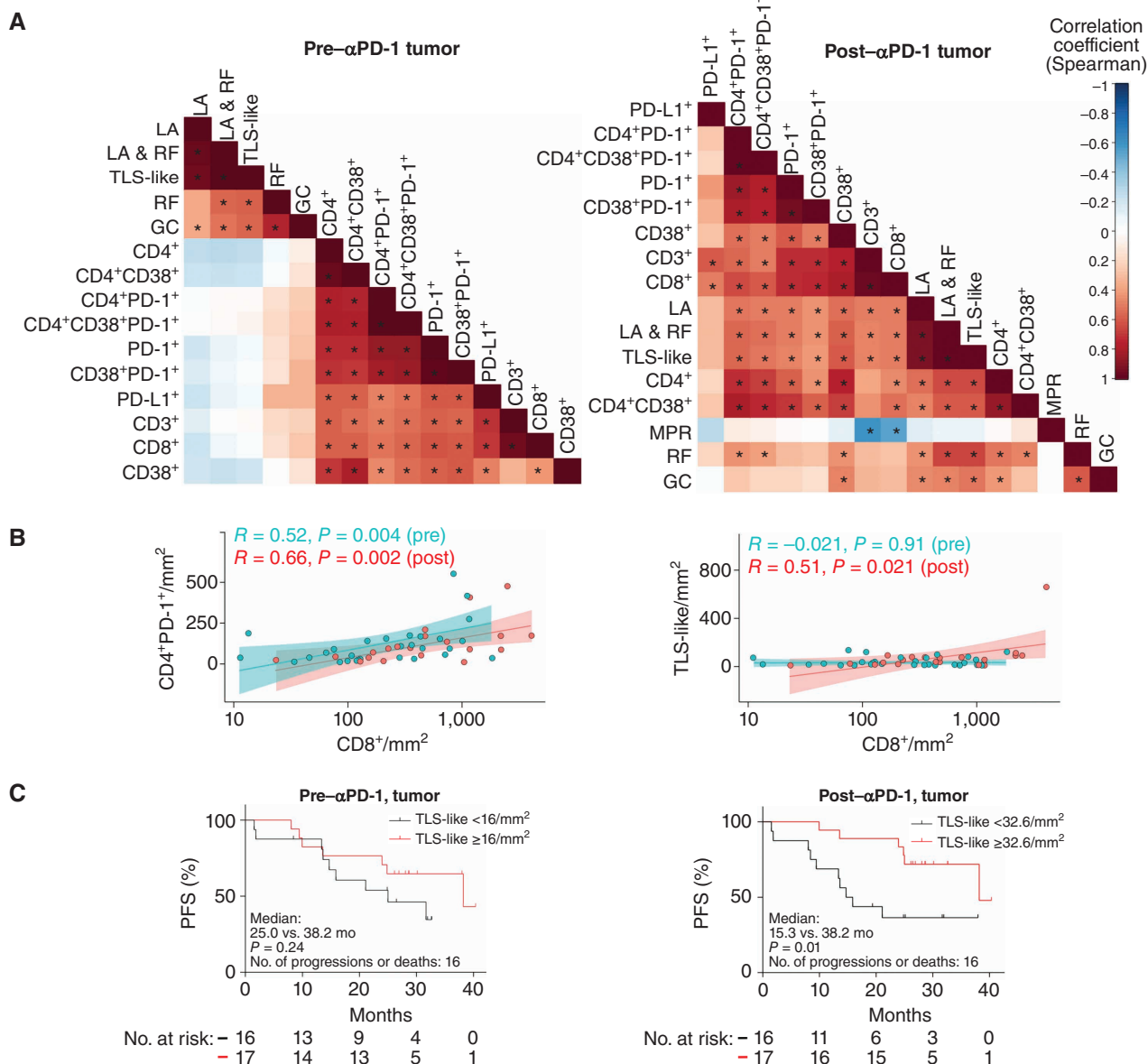


Figure 2. Blood T_{FH} and antibody-secreting cells (ASC) are associated with PFS in PANDORE patients. **A**, Spearman correlation matrices between histopathologic features before (left) and after (right) pembrolizumab in bladder samples. Significant correlations are indicated with a star. TLS-like corresponds to the sum of the densities of each submentioned structure. **B**, Detailed results for the correlations between the densities of CD8⁺ and CD4+PD-1⁺ TILs (left) or TLS-like (right) at baseline (blue) and after treatment (pink). Each dot represents one patient, and R and P values are indicated. **C**, Kaplan-Meier curves of PFS according to the density of TLS-like using medians as cutoff values, at baseline (left, median = 16/mm²) and after treatment (right, median = 32.6/mm²). Statistical analyses used the log-rank test. (continued on next page)

Downloaded from http://AACRjournals.org/cancerdiscovery/article-pdf/12/10/2280/pdf by York University user on 01 January 2024

of different CD4⁺ T helper (TH) and regulatory T (Treg) subpopulations based on the relative expression of PD-1 and effector/memory markers for the response to pembrolizumab (ref. 41; Supplementary Fig. S3A and S3B). The unsupervised PhenoGraph analysis of the PD-1-expressing clusters revealed that cluster 9 defined as CD4⁺PD-1⁺CD45RA⁻CD28⁺CD27⁺CD127⁺, which are central memory T cells (TCM), and cluster 13 defined as CD4⁺PD-1⁺CD45RA⁻CD28⁺CD27⁺CD127^{low}/− cells, which are effector memory T cells (TEM), were the only circulating TH cells associated with PFS at baseline (cluster 9, TCM) and after pembrolizumab (cluster 13, TEM;

Supplementary Fig. S3C and S3D). Focusing on specific fingerprints, we found that cluster 9 was selectively enriched for the canonical marker of T_{FH} (19% expressing CXCR5), whereas cluster 13 cells expressed the activation marker CD38 (46% CD38⁺, 9% CXCR5⁺; Supplementary Fig. S3B), suggesting that pembrolizumab may preferentially target and activate T_{FH}. Hence, we performed a more biased analysis, applying a manual gating to investigate the clinical significance for PFS of all blood CD4⁺ TH and B cells, before and after pembrolizumab (Fig. 2D–G; Supplementary Fig. S2G and S2H). Central memory T_{FH} (CD4⁺CXCR5⁺PD-1⁺TCM) and

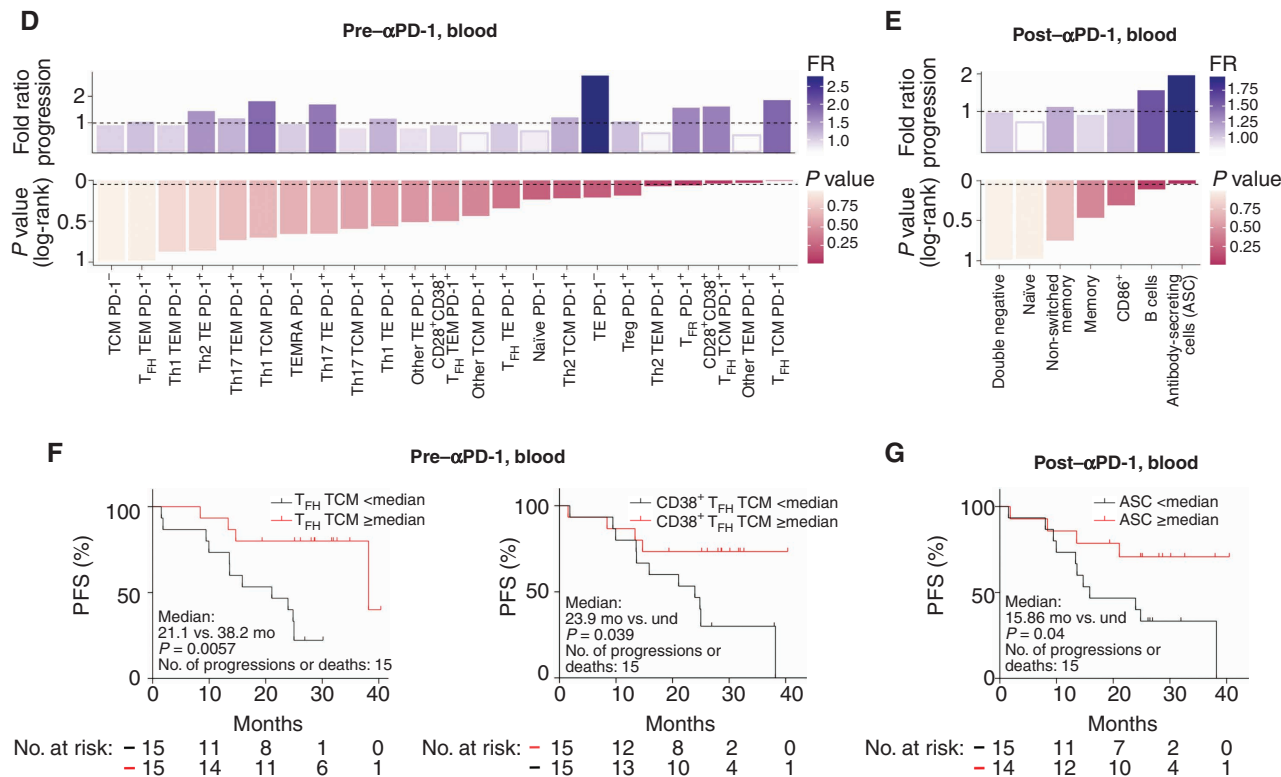


Figure 2. (Continued) **D** and **E**, Fold ratios (FR) between median values of each PD-1⁺ T-cell subset (**D**) or B cells (**E**) between nonprogressors versus progressors (top) and P values of log-rank tests (bottom) at baseline (**D**; also refer to Supplementary Fig. S2H) or after three cycles of pembrolizumab (**E**; also refer to Supplementary Fig. S2G) assessing the contribution of each CD4⁺ T-cell subset (**D**) or B cells (**E**) to PFS. CD4⁺ T-cell subsets were evaluated using mass cytometry ($n = 30$ samples) and a clustering method (PhenoGraph) followed by manual annotation and manual gating (refer to Supplementary Fig. S1A). B-cell subsets were evaluated using mass cytometry ($n = 29$ samples) followed by manual gating (refer to Supplementary Fig. S1B). TEMRA, effector memory T cells reexpressing CD45RA. **F** and **G**, Kaplan-Meier curves of PFS according to circulating T_{FH} TCM (left, median = 3.06%) and CD38⁺ T_{FH} TCM (right, median = 0.43%) in CD4⁺ T cells at baseline (**F**) or circulating ASCs (median = 0.05%) in CD45⁺ cells after three cycles of pembrolizumab (**G**), with medians as cutoff values. Statistical analysis used the log-rank test. und, undefined.

their activated fraction (CD38⁺CD28⁺CD4⁺CXCR5⁺PD-1⁺TCM) stood out as the most significant circulating TH cells predicting PFS at baseline (Fig. 2D and F; Supplementary Fig. S2G), whereas CD38^{hi}Blimp1⁺CD19^{+/lo} antibody-secreting cells (ASC) became associated with PFS only after pembrolizumab (Fig. 2E and G; Supplementary Fig. S2H).

Altogether, neoadjuvant pembrolizumab mostly benefited patients with MIBC who harbored preexisting T_{FH} TCM cells, which could orchestrate TLS-like formation and/or maturation as well as CD8⁺ T-cell tumor infiltration.

T_{FH} Accumulated within TLS-like and Predicted Prolonged PFS

We next measured the spatial distribution of T_{FH} in tumor lesions using multiplex immunofluorescence staining with mAbs specific for CD20, CD4, CD38, and PD-1 (Fig. 3A). Because T_{FH} are known to reduce CXCR5 expression when they infiltrate the tumor tissue (42), we defined T_{FH}-like cells as CD4⁺ T cells coexpressing CD38⁺ and PD-1. We found that the accumulation of T_{FH}-like triple-positive cells in the vicinity of TLS-like at baseline strongly correlated with PFS at 24 months (Fig. 3B; refer to Methods and Supplementary Fig. S2A–S2L). As shown with circulating T_{FH} TCM, the baseline density of intra-TLS T_{FH}-like triple-positive cells was associated with prolonged PFS (Fig. 3C). We corroborated

this accumulation using a CD4:Bcl6 costaining and did not observe differences between before and after treatment (Fig. 3D). Moreover, the density of such T_{FH}-like cells within the tissue correlated with TLS-like formation before but not after pembrolizumab (Fig. 3E, bottom vs. top). To further characterize T_{FH}-like cells within the tumor immune atlas after pembrolizumab, we performed CyTOF on 11 available tumors after cystectomy (Supplementary Table S3). As observed in blood, the CD38^{hi}CD28⁺ subset of nonregulatory PD-1⁺CD4⁺ T cells best predicted PFS among all the TIL subsets (Supplementary Fig. S4A and S4B and gating strategy in Supplementary Fig. S3) and correlated with B lymphocytes (Supplementary Fig. S4C).

In addition, we performed single-cell RNA sequencing (RNA-seq) of blood CD45⁺ cells and tissue leukocytes from two tumor-free bladders, harvested from surgical specimens of a patient with pCR and PFS ≥ 24 months (P#38) and one MIBC from a nonresponding patient with progressive disease (P#02; Supplementary Table S4). The unsupervised clustering of cell heterogeneity identified one cluster (cluster 2) enriched in CD4⁺ TILs (Fig. 3F; Supplementary Fig. S5A–S5C). The CD38-, CD28-, and PD-1-specific oligo-conjugated antibodies allowed us to measure the expression of the prototypical transcript of T_{FH} cells, CXCL13, only in the CD4⁺ TIL fraction of the patient exhibiting a pCR (Fig. 3F, right).

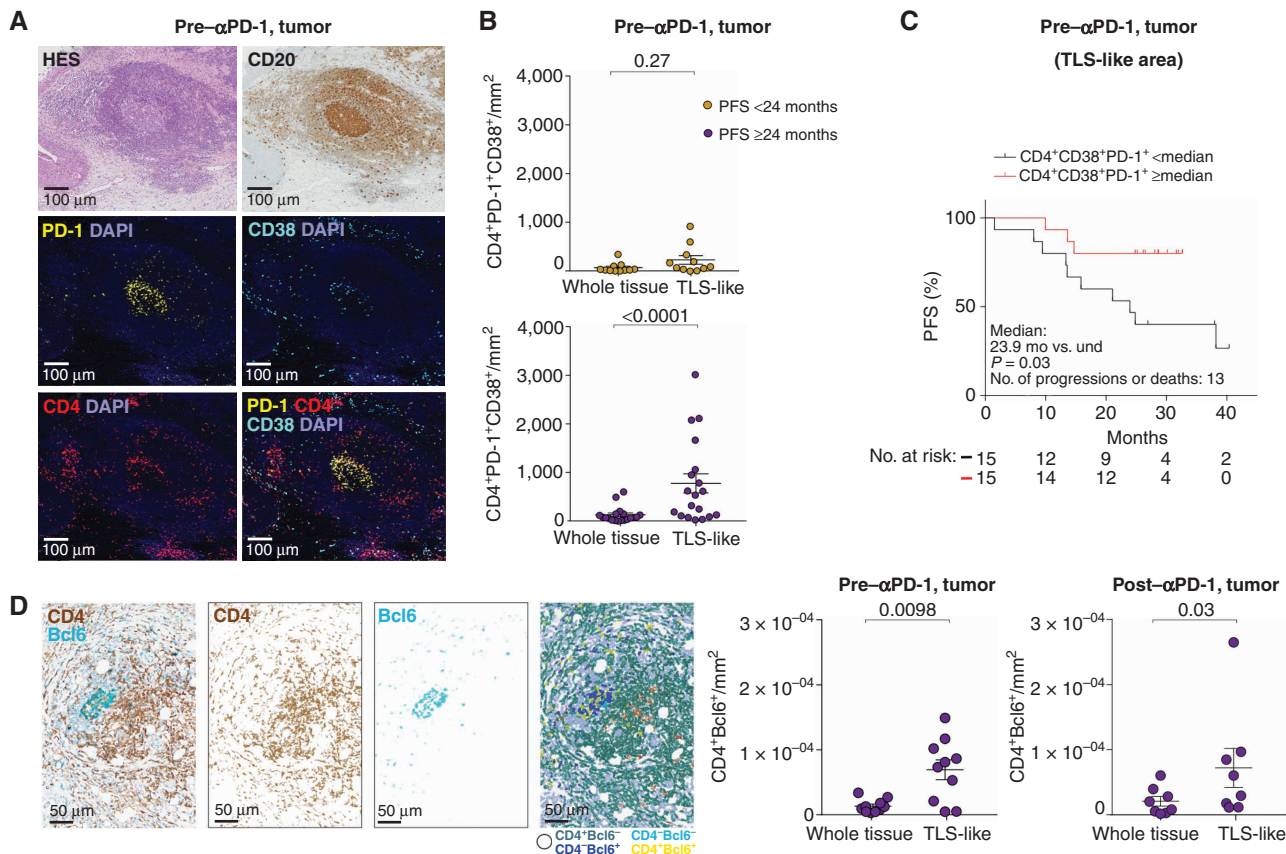


Figure 3. Tumoral T_{FH} -like CD4+ T cells are associated with TLS-like and predict PFS. **A**, Representative micrograph of a mature TLS on HES (top left), constituted by CD20+ cells evidenced by IHC (top right), and of single (middle and bottom left) and triple-positive CD4+CD38+PD-1+ analyzed by immunofluorescence stainings (bottom right) in a radical cystectomy specimen from a patient with PFS ≥24 months (P#39). **B**, Accumulation of CD4+CD38+PD-1+ in TLS-like compared with whole tissue before treatment (refer to Methods). Data are shown as mean ± SEM. Each dot represents one patient, and color indicates the PFS status at 24 months (purple: absence of relapse and/or death at 24 months; gold: relapse and/or death at 24 months). Statistical analysis used paired t tests (paired Wilcoxon test). **C**, Kaplan-Meier curve of PFS according to CD4+CD38+PD-1+ cells in TLS-like (median = 222/mm²) at baseline in TURBT using medians as cutoff values. Statistical analyses used the log-rank test. und, undefined. **D**, Representative micrograph of TLS-like using CD4 and Bcl6 colabeling analyzed by IHC in a specimen pre-pembrolizumab (TURBT) from a patient with PFS ≥24 months (P#24; left). Left, original image for CD4:Bcl6 is shown (10 \times), followed by color deconvolution for CD4 and Bcl6 channels and a final image corresponding to cell detection done by QuPath based on color deconvolution. Accumulation of CD4+Bcl6+ in TLS-like compared with whole tissue before and after treatment (refer to Methods, "Evaluation of CD4+Bcl6+ cells"). Data are shown as mean ± SEM. Each dot represents one patient without relapse and/or death at 24 months (right). Statistical analysis used paired t test (paired Wilcoxon test). (continued on next page)

To better dissect the T_{FH} phenotype, we set up new panels of multidimensional flow cytometry, including CXCR5, CXCL13, and Bcl6, in addition to CD38, PD-1, CD40L, and ICOS to comprehensively define the T_{FH} -like cells in seven freshly dissociated MIBCs at diagnosis. A representative flow-cytometric analysis and gating strategy are depicted in Supplementary Fig. S4. As outlined in Supplementary Table S5, the subset of conventional ($Foxp3^-$) CD4+ TILs (convCD4+ T cells) coexpressing PD-1 and CD38 is by and large the same as the PD-1+ICOS+ double-positive one [representing $17.5\% \pm 3.9$ and $17.2\% \pm 3.0$ (mean ± SEM) of convCD4+ TILs, respectively], comprising 27% to 73% of CXCL13+ and 64% to 76% CD40L+ cells (IQR; Supplementary Fig. S6A and S6B). The median fluorescence intensity (MFI) of Bcl6 increased gradually—from MFI = 112 for all convCD4+ T cells up to MFI = 149 for PD-1+CD38+ convCD4+ T cells (compared with MFI = 96 in the PD-1-CD38- double-negative convCD4+ subset), culminating in an MFI = 155 for PD-1+ICOS+ convCD4+ TILs (mean values; Supplementary Fig. S6A and

S6B; Supplementary Table S5). In addition, CXCR5 and CXCL13 expressions appeared mutually exclusive, suggesting endocytosis of the receptor upon CXCL13 binding and engagement with CXCR5 (Supplementary Fig. S6C).

Finally, to determine which TH cell-related soluble hallmark could be induced by pembrolizumab, we monitored the dynamic circulating levels of 40 soluble immune and nonimmune factors by bead-based multiplex assay prior to, during, and after pembrolizumab in 38 patients. We found that CXCL13 stood out as the most significant chemokine systemically released in blood after the first cycle, and this early rise was associated with the absence of progression at 24 months, as opposed to other Th1 markers (such as CXCL9) that tended to increase in all patients (Fig. 3G and H; Supplementary Fig. S5D, left). Of note, CCL19, a homeostatic chemokine involved in the architectural organization of TLS (43, 44), accompanied the rise of CXCL13 and was associated with prolonged PFS (Supplementary Fig. S5D, right; Supplementary Fig. S5E, left), whereas CXCL8 predicted

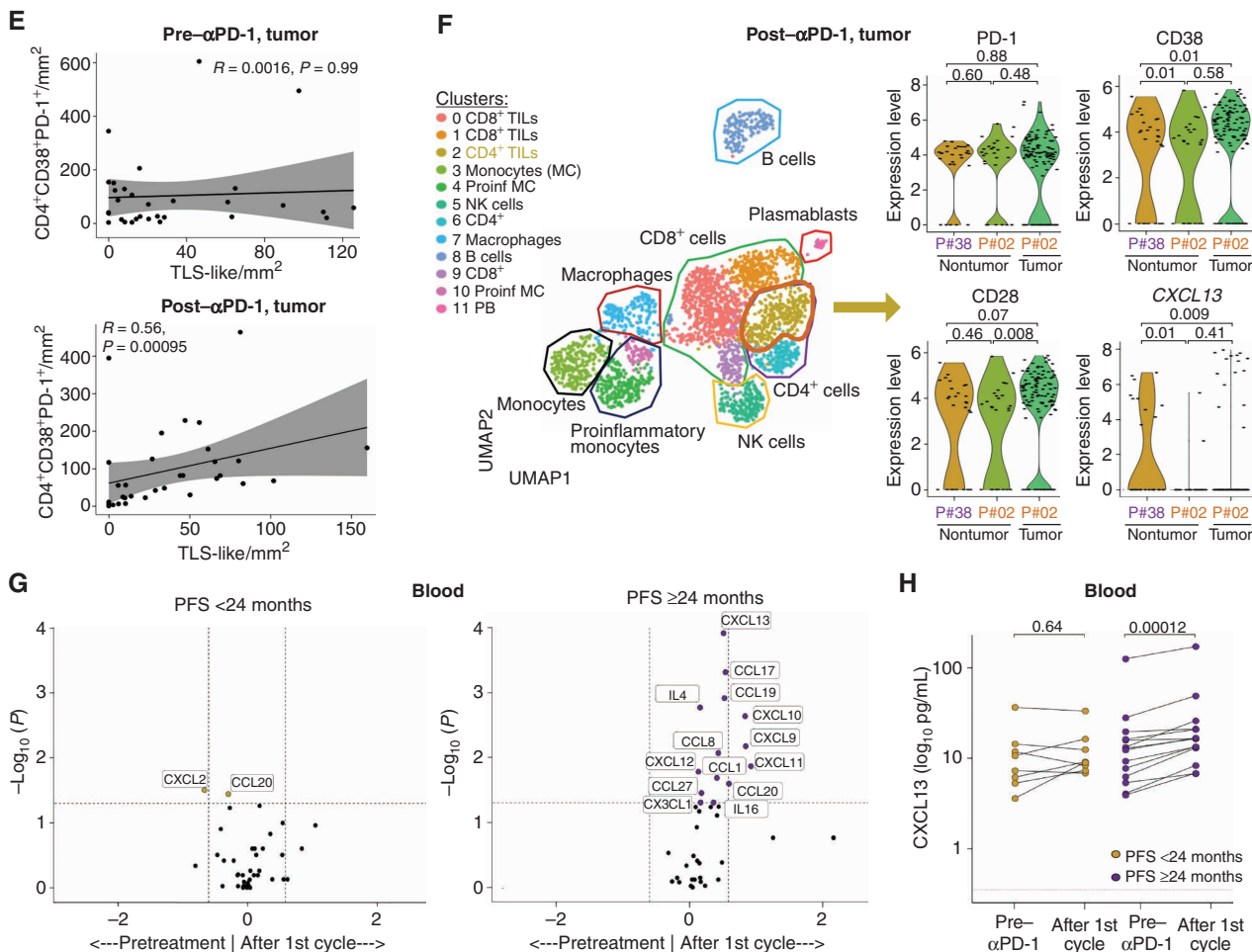


Figure 3. (Continued) **E**, Spearman correlations between CD4⁺CD38⁺PD-1⁺ cells and TLS-like in bladder tissues at baseline (top) and after 3 cycles of pembrolizumab (bottom). Each dot represents one patient. **F**, Single-cell transcriptomics of CD45⁺ in four radical cystectomy specimens and two peripheral blood mononuclear cell (PBMC) samples. Analysis of Rhapsody single-cell RNA-seq data, displayed by uniform manifold approximation and projection (UMAP; left). Seurat clustering of 2,432 CD45⁺ cells from primary bladder tumors, surrounding nontumoral tissue and PBMCs. Expression levels of the CXCL13 gene product in CD4⁺ TILs (cluster 2) depicted in violin plots, as well as of PD-1, CD38, and CD28 at the protein level in three specimens collected after anti-PD-1 mAbs [healthy bladder tissue from complete responder (P#38), healthy bladder tissue and bladder cancer from nonresponder (P#02)]. NK, natural killer; PB, plasmablast; Proinf, proinflammatory. **G**, Multiplex array of inflammatory analytes in the plasma. Volcano plots showing differential plasma concentrations of cytokines/chemokines before and after one cycle of pembrolizumab in the group of patients experiencing or not a relapse and/or death before 24 months (left and right, respectively). Volcano plots were generated computing for each soluble factor: (i) the log₁₀ of fold ratio among the mean values after normalization, after first injection versus preinjection of pembrolizumab (x-axis), and (ii) the log₁₀ of *P* values deriving from the paired Wilcoxon test calculated in absolute values (y-axis). Black and colored dots are considered nonsignificant (*P* < 0.05) or significant (*P* > 0.05), respectively. **H**, Plasma concentration of CXCL13 (log₁₀) in pre- versus post-first cycle of pembrolizumab in the two groups (according to PFS status at 24 months). Each line represents one patient. The dotted line indicates the lower detection threshold of CXCL13. Statistical analysis used paired t test (paired Wilcoxon test).

resistance to therapy (Supplementary Fig. S5E, right), as already described in lung cancer (45).

These results suggest that in patients with prolonged PFS, PD-1 blockade using pembrolizumab may have facilitated the accumulation of T_{FH}-like cells in TLS and induced the release of the T_{FH}-prototypic CXCL13 chemokine in tissue lesions and the bloodstream of patients.

MIBC-Residing T_{FH} Are Associated with Ex Vivo Responses to Pembrolizumab

Next, we asked if T_{FH} cell accumulation within TILs is a prerequisite for the immunologic response of MIBC to pembrolizumab. We used the *in vitro/in situ* (“*in vitro*”) assay that we recently developed to search for surrogate markers

of immune reactivity to ICBs (refs. 46, 47; Fig. 4A). Hence, we assessed the *ex vivo* immunoreactivity to pembrolizumab of 18 surgical resections of MIBC specimens (56% pT3) from treatment-naïve patients (Supplementary Table S6; Fig. 4A). To calculate the index of immune stimulation by anti-PD-1 mAbs, we normalized raw values onto medium values, those being mostly equivalent to isotype control mAb-related values (46). We used nonsupervised hierarchical clustering of z score-normalized concentrations of 28 immune- and nonimmune-soluble factors monitored by bead-based multiplex assay and ELISA, as previously described (46). The heat map of this clustering highlighted two categories of patients with MIBC: 22% (*n* = 4/18) exhibiting increased levels of most analytes above the mean of

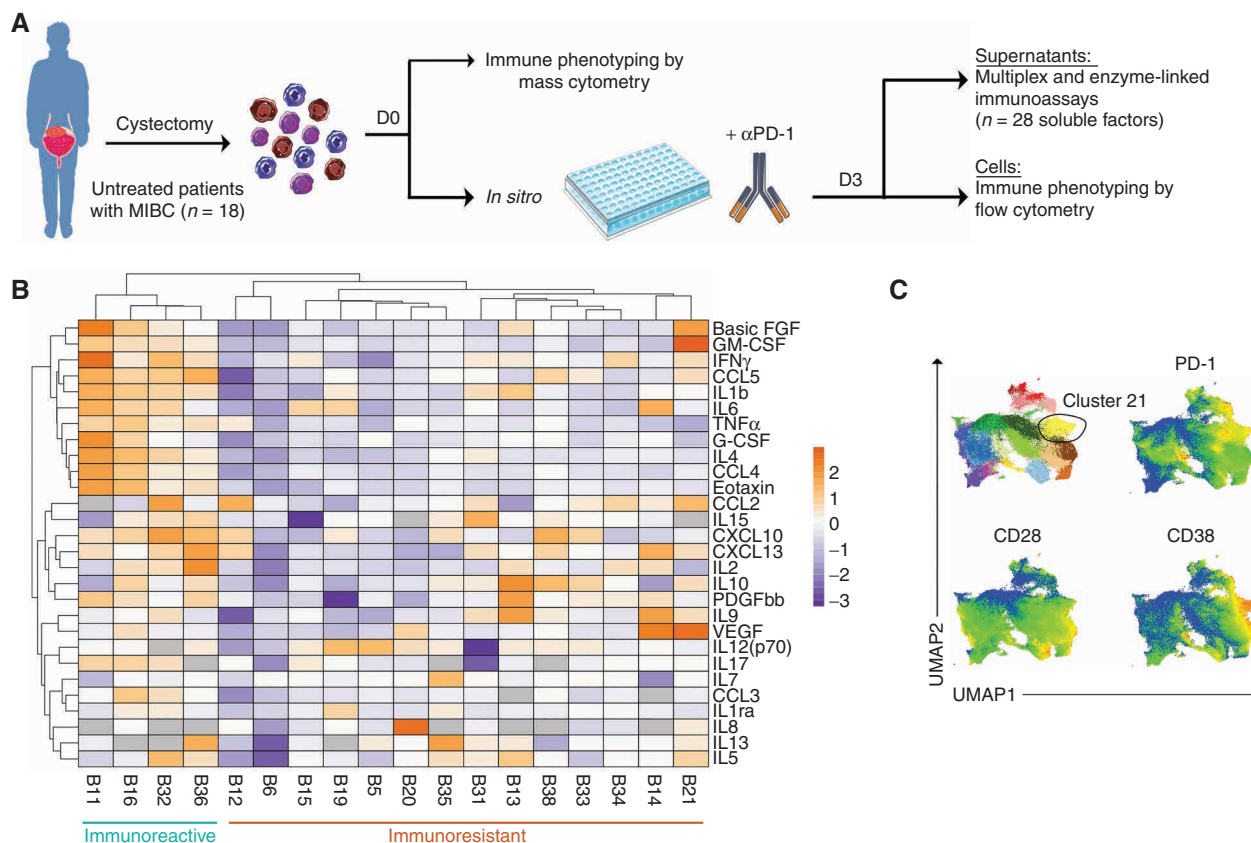


Figure 4. Preexisting T_{FH} -like $CD4^+$ T cells are prerequisites for a functional response of MIBC to pembrolizumab *ex vivo*. **A**, Overview of the *in situ* (*in vitro*) test. **B**, Heat map of the nonsupervised hierarchical clustering ($n = 18$) of 28 soluble factors (including CXCL13 monitored in ELISA) secreted from MIBC exposed to 72 hours of pembrolizumab. Missing values are shown in gray. Both rows and columns are clustered using correlation distance and average linkage. **C**, Uniform manifold approximation and projection (UMAP) showing the PhenoGraph clusters (refer to Supplementary Fig. S6A) of $CD4^+$ TILs in 18 untreated bladder cancers (mostly MIBC, $n = 17/18$) analyzed by mass cytometry (top left) at day 0. Cluster #21 is surrounded by a circle. Relative expression of PD-1 (top right), CD28 (bottom left), and CD38 (bottom right) in $CD4^+$ TILs at day 0, displayed by UMAP. (continued on next page)

Downloaded from http://aacjournals.org/cancerdiscovery/article-pdf/12/10/2280/3211219/2280.pdf by York University user on 21 January 2024

the whole cohort after stimulation with anti-PD-1 mAbs (called henceforth “immunoreactive,” Fig. 4B), and 88% who failed to do so. The most significant differences between immunoreactive and nonimmunoreactive tumors resided in the release of Th1/Th2 hallmarks (CXCL10, IFN γ , GM-CSF, CCL4, CCL5, eotaxin, and IL4) compatible with the T-cell receptor cross-linking secretory profile (46) as well as inflammatory cytokines (IL1 β , TNF α , and IL6; Fig. 4B). We then examined correlates between *in vitro* immunoreactivity and basal CyTOF-based unsupervised clustering using PhenoGraph in these 18 MIBCs. Tumor-infiltrating $CD4^+$ TEM cells ($CD45RA^-CD127^-CD28^{+int}$) harboring high expression levels of PD-1, CD38, and CD28 with coexpression of activation markers ($CD69^{+}CD95^{+}CD39^{+}$) belonging to clusters 21 and 28 best predicted *in vitro* responsiveness to PD-1 blockade (Fig. 4C and D; Supplementary Fig. S7A and S7B). We next performed single-cell RNA-seq on two independent MIBC-infiltrating $CD45^+$ leukocyte populations at baseline [harvested from an immunoreactive tumor (B#11) and a tumor at the edge between nonimmunoreactive and nonimmunoreactive (B#12)]. Here again, within the cluster that mostly comprised $CD4^+$ TILs (cluster 2; Supplementary Fig. S5B), membrane expression of CD38, CD28, and PD-1

molecules allowed us to identify the T_{FH} pathognomonic transcript, CXCL13, in the $CD4^+$ TILs (Fig. 4E), suggesting that CXCL13-T $_{FH}$, which expressed PD-1, are critical to potentiate the induction of immune reactivity to *ex vivo* PD-1 blockade. Supporting this finding, the percentages of baseline $CD4^+CD38^{hi}CD28^{+PD-1^{hi}}$ TILs (clusters 21 and 28, differing for their expression of CD103 and relative expression of CD28) and spontaneous CXCL13 release correlated among each other, and all were markedly higher in immunoreactive compared with nonimmunoreactive MIBC (Fig. 4F; Supplementary Fig. S7C). Of note, CXCL13-expressing $CD8^+$ T cells were detectable but failed to segregate immunoreactive from nonimmunoreactive tumors (Supplementary Fig. S8A). In parallel, the unsupervised clustering of tumor-infiltrating $CD8^+$ T cells (Supplementary Fig. S8B and S8C) showed positive correlations between T_{FH} TILs (cluster 21) and $CD38^{hi}CD39^{hi}PD-1^{hi}TIGIT^{+}CD69^{+}CD103^{+}$ tissue-resident $CD8^+$ TILs (TRM; Supplementary Fig. S8C and S8D, top) but not with $CD8^{+}CD38^{-}CD39^{-}PD-1^{+}$ tissue-resident TILs (clusters CD8 $^{+}$ 24 and 12) or non-tissue-resident $CD8^+$ TILs (cluster CD8 $^{+}$ 30; Supplementary Fig. S8C and S8D, bottom). Although CD38 was used as a proxy marker to identify the CXCL13-expressing PD-1 $^{+}$ T_{FH} $CD4^+$ TIL subset, CD38

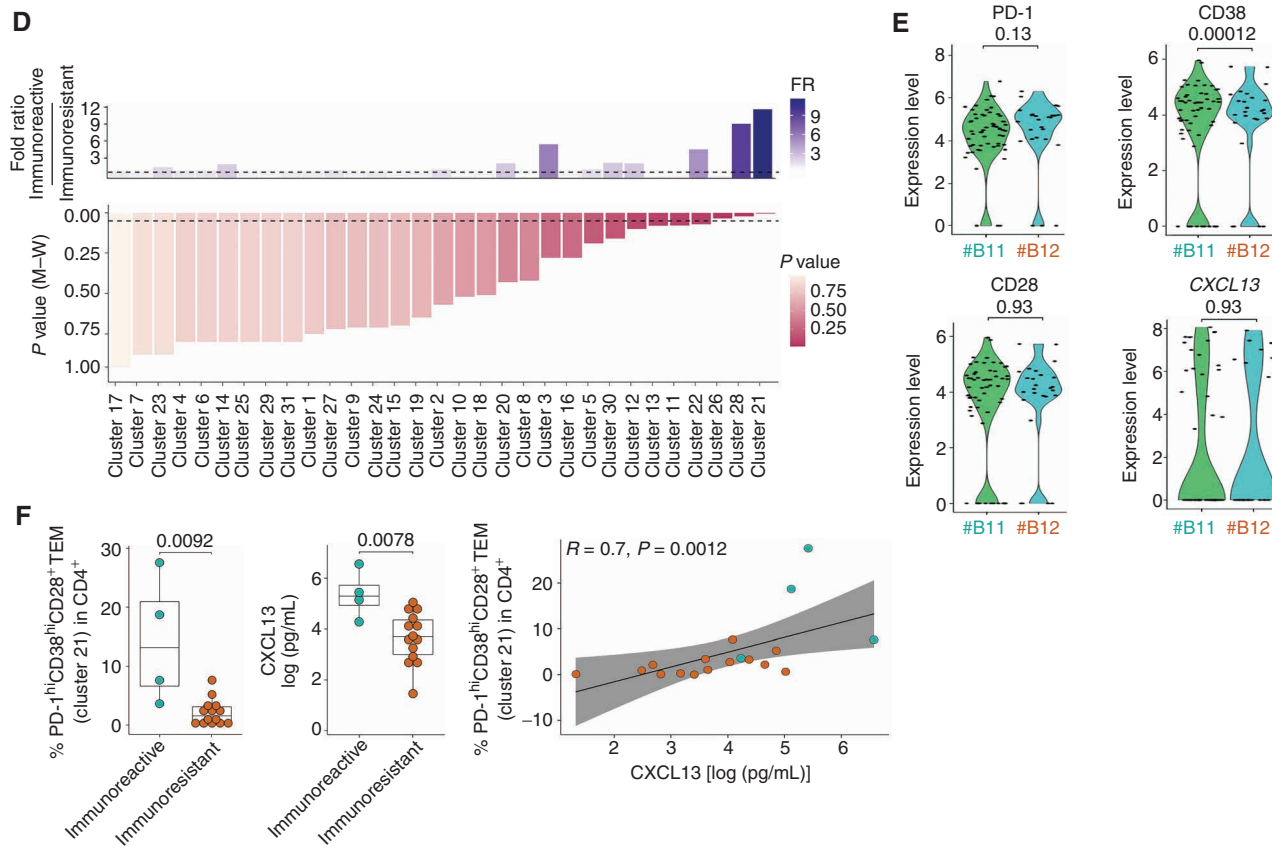


Figure 4. (Continued) **D**, Bar chart showing fold ratio of median CD4⁺ TIL cluster values between immunoreactive versus nonimmunoreactive MIBC (top). Increasing blue gradient for increased fold ratios (FR). Bar charts showing the *P* values of unpaired *t* test [Mann–Whitney (M-W) *U* test] for each CD4⁺ TIL cluster (bottom). **E**, Expression levels of the CXCL13 gene product in CD4⁺ TILs (cluster 2, as shown in Fig. 3E) depicted in violin plots, as well as PD-1, CD38, and CD28 at the protein level in two specimens collected before the *in vitro* assay. Samples from untreated patients were utilized (#B11: immune-reactive tumor, #B12: at the edge between immunoresistant and immune-reactive tumors). **F**, Percentages of CD38^{hi}CD28⁺PD-1^{hi} (cluster 21) in CD4⁺ TILs (left), quantification of CXCL13 production after 3 days of *in vitro* assay without treatment (middle), and Spearman correlation between both parameters (right). Box plots display a group of numerical data through their third and first quartiles (box), mean (central band), and minimum and maximum (whiskers). Each dot represents one tumor. Statistical analyses used unpaired *t* test (Mann–Whitney *U* test).

did not behave as a checkpoint inhibitory molecule, because we failed to increase or trigger TIL immunoreactivity by combining anti-CD38 with anti-PD-1-neutralizing mAbs in the *in vitro* system (Supplementary Fig. S8E).

Although further work is needed to evaluate the clinical significance of CD8⁺ TILs during neoadjuvant pembrolizumab, PANDORE and *in vitro* studies both converged in showing that pembrolizumab potentiated the TLS-associated anti-tumor activity by coordinating T_{FH}, B cells, and CD8⁺ TRM.

T_{FH} Are Key Targets of Pembrolizumab among CD4⁺ T Cells

Visualizing the molecular targets of the pembrolizumab IgG4 antibody is of the utmost importance for determining the mechanisms of action of this drug. Although many investigators identified CD8⁺ cells as the main functional targets of anti-PD-1 mAbs (10, 48, 49), we took a comprehensive approach to study IgG4⁺ cells in the blood and within cystectomy tissues using CyTOF and immunofluorescence analyses. We confirmed that among blood CD4⁺PD-1⁺ cells, CD4⁺ TEM (cluster 13), as well as TE (clusters 5 + 15) and to a lesser extent TCM (clusters 6 + 9 + 20)

exhibited the strongest binding to anti-IgG4 mAbs during pembrolizumab treatment (Fig. 5A and B; Supplementary Fig. S9A–S9C). Moreover, we found a higher proportion of IgG4⁺ cells in the CD28⁺CD38⁺PD-1⁺ TEM T_{FH}-like subset (cluster 13) before the third injection of pembrolizumab in patients with a prolonged clinical benefit compared with patients with PFS <24 months (Fig. 5C). In tumor beds, IgG4 binding to CD38⁺ T_{FH}-like was particularly intense within tumor areas enriched in TLS-like (Fig. 5D and E). To better ascribe the IgG4 staining to the therapeutic Ab and not to a local B-cell Ig switch, we compared the dynamics of IgG4 staining in various subsets of MIBC-residing cells before and after pembrolizumab. There was a significant rise only in the CD4⁺IgG4⁺ subset after therapy (Fig. 5F). Next, we performed stainings with anti-IgG and anti-IgA antibodies on MIBC samples before and after pembrolizumab and found a preferential labeling of plasma cells with an increase of IgG at the expense of IgA in tumor beds, resulting in a significant pembrolizumab-associated rise in the IgG/IgA ratio (Fig. 5G). In contrast, the IgG/IgA ratio remained stable in the periphery (Fig. 5H). After 3 days of *in vitro* stimulation with anti-PD-1 mAbs, the MFI of IgG4 in

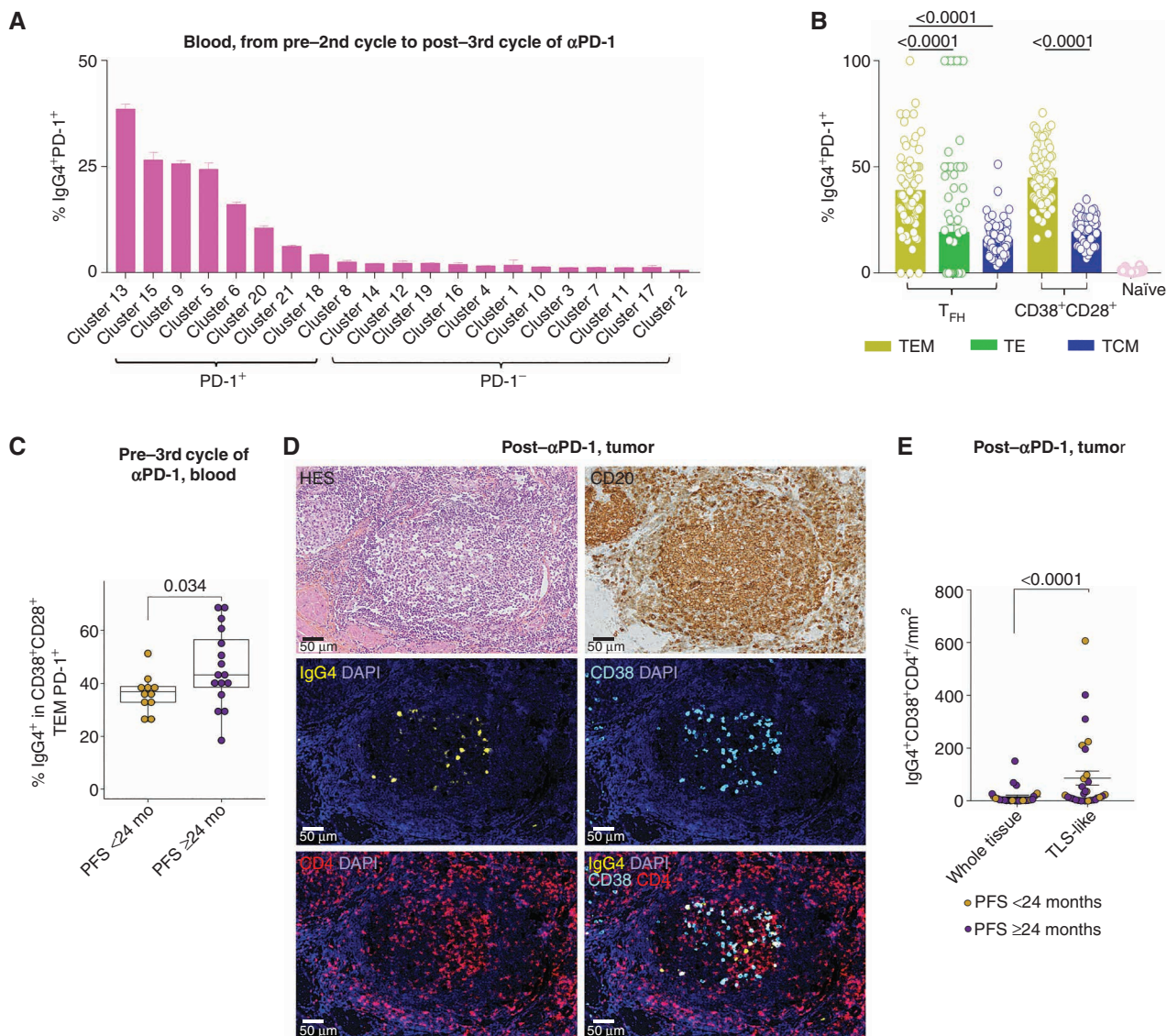


Figure 5. Preferential binding of pembrolizumab to T_{FH} and CD38⁺CD28⁺ T_{FH}-like cells. **A**, Unbiased analyses of IgG4⁺PD-1⁺ within each cluster of peripheral CD4⁺ T-cell subset. For each cluster, the average of mean values at three time points for all patients [pre–second, pre–third, post–third cycle (before surgery) of pembrolizumab] as well as the standard error of means are depicted. **B**, Frequencies of peripheral IgG4⁺PD-1⁺ within activated (CD38⁺) TCM, TEM, T_{FH} TCM, T_{FH} TEM, and T_{FH} TE as well as in naïve CD4⁺ T cells as negative control at three time points for all patients [pre–second, pre–third, post–third cycle (before surgery) of pembrolizumab]. Each dot represents one sample. Statistical analysis used the Kruskal–Wallis test. **C**, Frequencies of peripheral IgG4⁺PD-1⁺ in activated CD38⁺ TEM before the third injection of pembrolizumab in the group of patients experiencing PFS < or ≥24 months. Box plots display a group of numerical data through their third and first quartiles (box), mean (central band), and minimum and maximum (whiskers). Each dot represents one patient. Statistical analysis used an unpaired t test (Mann–Whitney U test). **D**, Representative micrograph of TLS-like on HES (top left), constituted predominantly by CD20⁺ cells evidenced by IHC (top right) and of single (middle and bottom left) and triple-positive CD4⁺CD38⁺IgG4⁺ cells by immunofluorescence stainings (bottom right) in a radical cystectomy specimen from a patient with PFS ≥24 months (P#39). **E**, Accumulation of CD4⁺CD38⁺IgG4⁺ T_{FH}-like in TLS-like compared with whole tissue after treatment (refer to Methods, “Geodistribution of CD4⁺CD38⁺PD-1⁺ and CD4⁺CD38⁺IgG4⁺ T_{FH}-like in FFPE samples”). Box plots display a group of numerical data through their third and first quartiles (box), mean (central band), and minimum and maximum (whiskers). Each dot represents one patient (gold: relapse and/or death, purple: absence of relapse and/or death). Statistical analysis used paired t tests (paired Wilcoxon test). (continued on next page)

Downloaded from http://aacjournals.org/cancerdiscovery/article-pdf/12/10/2280/3211219/2280.pdf by York University user on 21 January 2024

CD38^{hi} and CD38^{lo} subsets revealed a trend for preferential binding to CD38^{hi}-expressing CD4⁺ TILs in immunoreactive tumors (Supplementary Fig. S9D, top). As expected, there was a correlation between IgG4 and PD-1 positivity on this CD38^{hi}CD4⁺ T-cell subset after pembrolizumab (Supplementary Fig. S9D, bottom). Of note, supernatants of the *in vitro* studies contained higher baseline levels of IgA and

IgG1, IgG2, or IgG than IgE, IgG3, and IgG4 (Supplementary Fig. S10A) that did not increase within 72 hours despite a rise in ASCs after bacterial stimulation (Supplementary Fig. S10B).

Altogether, within CD4⁺ T cells, pembrolizumab preferentially targeted circulating and tumor-associated T_{FH} expressing CD38 and residing in TLS-like area.

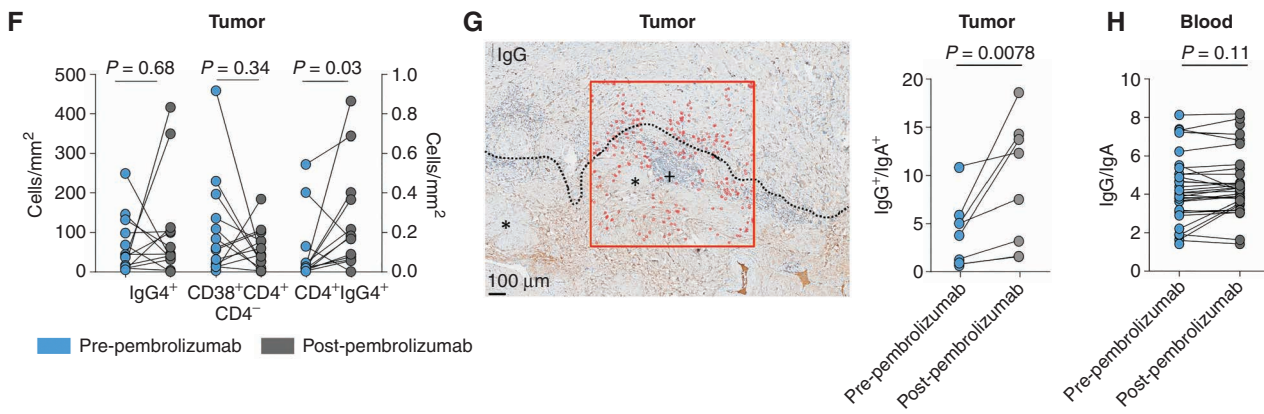


Figure 5. (Continued) **F**, Densities of IgG⁺, CD4⁻CD38⁺IgG⁺ cells (left y axis of the right) and CD4⁺IgG⁺ cells (right y axis of the right) computed and counted from multiplex-labeled slides before (blue) or after (gray) pembrolizumab in 13 paired patients. Statistical analysis used paired t tests (paired Wilcoxon test). **G**, Representative micrograph of IgG⁺ cells in one out of five regions of interest (red rectangle; magnification 10 \times). IgG- and IgA-positive cells, mainly corresponding to plasma cells, were counted in five regions of interest in similar peritumoral areas of MIBC in sequential slides in order to generate IgG and IgA density (left). +, TLS; *, smooth muscle. Tumor is delineated by discontinuous line (tumor on the top). Ratio of IgG⁺/IgA⁺ cells in bladder tissues before and after treatment evaluated by IHC in eight paired PANDORE cases (right). Statistical analysis used paired t tests (paired Wilcoxon test). **H**, Ratio of soluble IgG/IgA in patient serum before and after treatment. Statistical analysis used paired t tests (paired Wilcoxon test).

E. coli-Specific Memory T_{FH} and B-cell Responses Are Associated with Clinical Benefit to Neoadjuvant Pembrolizumab

Urine is not sterile, and commensal bacteria are present in the urinary tract of both healthy patients and patients with UC (50, 51). Indeed, patients with UC are commonly diagnosed with urinary tract infections (UTI) or asymptomatic bacteriuria (52). Uropathogenic bacteria have the capacity to invade bladder epithelial cells and can persist for prolonged periods of time (53, 54). Of note, the risk of developing UC in women is inversely correlated with UTIs (55). Additionally, patients diagnosed with noninvasive UC are treated by intravesical bacterial extracts [namely, Bacillus Calmette-Guérin (BCG)], which was the case for 17.9% ($n = 7/39$) of patients enrolled in the PANDORE study. Recent evidence indicates that local and intratumoral microbiota influence the prognosis of cancers developing at mucosal surfaces (56–59). Therefore, we investigated the presence of tumor-associated bacteria in MIBC using IHC [anti-lipopolysaccharide (LPS) staining], FISH, electron microscopy, qPCR, and culturomics in aerobic and anaerobic conditions. LPS⁺ structures within UC cells and/or immune cells were observed in up to 70% of TURBT ($n = 24/33$; Fig. 6A and B), coinciding with cytoplasmic granular structures and exceptionally with neutrophils (Supplementary Fig. S11A). These granular structures were more numerous in tumor cells than in normal urothelial cells from surrounding tumor-free tissues and might correspond, at least partially, to Gram⁺ bacteria that we isolated in most of the fresh MIBCs that we cultivated ($n = 6$; Fig. 6C and D). In particular, culturomics of primary bladder tumors and surrounding noncancerous tissues allowed us to identify *Staphylococcus capitis*, *Cutibacterium acnes*, and *Corynebacterium tuberculostearicum* in the tumor tissues but not in the transport supernatant of the tumor, suggesting that these Gram⁺ bacteria were not contaminants (Fig. 6D; Supplementary Fig. S11B). Given the ability of *E. coli* to invade urothelial cells, we ran qPCR using *E. coli*-specific probe sets (53, 54) and

could detect specific signals in 70% of the cases ($n = 14/20$ of total cases with $n = 7/11$ untreated specimen and $n = 7/9$ post-pembrolizumab) without differences between tumors and surrounding “healthy” tissues (Fig. 6E and F). FISH using specific probes for 16s rRNA, *E. coli*, and uropathogenic *E. coli* (UPEC; ref. 60) allowed us to visualize UPEC in tumor, nontumoral urothelium, and immune cells (Fig. 6G). Finally, we confirmed the presence of live bacilli within bladder tissues by scanning and transmission electron microscopy, either intracellularly or in intercellular spaces (Fig. 6H, right and left). Of note, we found a strong correlation between neutrophils and ASCs within tumor-infiltrating CD45⁺ cells after pembrolizumab (Fig. 6I), suggesting that innate and humoral immune responses against bacteria might cooperate in the tumor beds.

Hence, we addressed whether memory T- or B-cell immune responses directed against *E. coli*, BCG, and other urinary bacterial species such as *Corynebacterium tuberculostearicum* and *Cutibacterium acnes* could be detected before and after pembrolizumab. We first performed a longitudinal study of blood CD4⁺ T-cell recall responses against urinary tract and tumor bacteria, monitoring cytokines prototypic of Th1 (IFN γ), T_{FH} (CXCL13), and regulatory (IL10) T-cell responses (refs. 61–63; Supplementary Table S7; Fig. 7A). Patients with UC harbored preexisting commensal-specific Th1 and T_{FH} memory T-cell responses that tended to increase and decrease by pembrolizumab for the former and the latter, respectively (Fig. 7B; Supplementary Fig. S11C and S11D). Interestingly, baseline CXCL13-producing T_{FH} but not IFN γ -releasing Th1 memory T-cell responses against *E. coli*, and not *S. capitis*, were associated with the absence of progression at 24 months (Fig. 7B; Supplementary Fig. S11D). Of note, there was no CXCL13 release after stimulation with LPS or lipoteichoic acid (LTA; Supplementary Fig. S11E). We next analyzed the *in situ* reactivity to *E. coli* with or without pembrolizumab in *in vitro* assays on fresh MIBC (Fig. 7C, top). After 72 hours of exposure to heat-inactivated *E. coli*, we observed a release of CXCL13

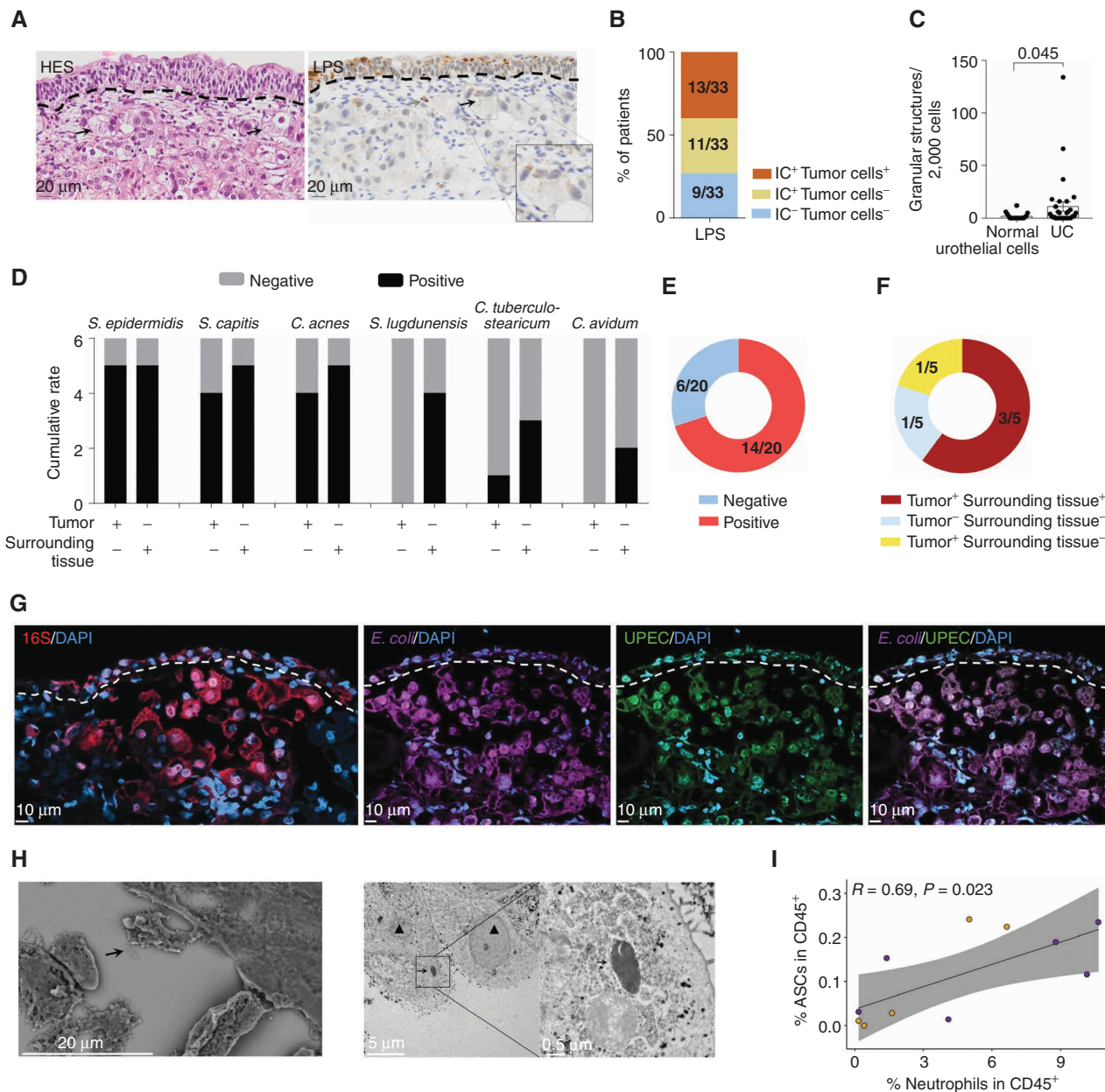


Figure 6. MIBCs contain Gram-negative bacteria with uropathogenic capacities. **A**, Representative micrograph of one bladder showing nontumoral urothelium (above discontinuous line) with invasive cells of UC containing granular cytoplasmic structures (arrows) in P#43 in HES at 20× magnitude (left). LPS IHC staining of the same area highlighting granular cytoplasmic positivity in the normal urothelium, immune cells (gray arrow), and tumor cells (black arrow) at 20× magnitude. **B**, Proportions of patients with positive or negative LPS staining in immune cells (IC) and tumor cells ($n=33$ patients). **C**, Enumeration of granular cytoplasmic structures in normal and tumoral urothelium. Each dot represents one patient sample. Statistical analysis used unpaired t tests (Mann-Whitney U test). **D**, Stacked bar chart showing bacteria cultivated by culturomics (refer to Methods) within tumor and nontumor tissues ($n=6$ patients with paired tissues). Total number of positive (black) or negative (gray) samples is depicted. *C. avidum*, *Cutibacterium avidum*; *S. epidermidis*, *Staphylococcus epidermidis*; *S. lugdunensis*, *Staphylococcus lugdunensis*. **E**, Proportions of samples with positive or negative PCR detection of *E. coli* ($n=20$ bladder specimens, with $n=9/20$ post-pembrolizumab and $n=11/20$ untreated). **F**, Proportions of patients with paired samples of tumor and surrounding nontumor tissues ($n=6$ untreated patients) for PCR detection of *E. coli*. **G**, Distribution of bacteria, *E. coli*, and UPEC by FISH in the same area shown in **A** with *E. coli* (middle left), UPEC-specific probes (middle right) and merge (right) at 40× magnitude. **H**, Scanning (left) and transmission (right) electron microscopy illustrating bacilli (arrow) morphologically compatible with Enterobacteriaceae in the intercellular space (left) or within an urothelial tumor cell (right) in P#08 (left) and P#18 (right). Triangle indicates nucleus. **I**, Spearman correlation between ASCs and neutrophils in tumoral CD45⁺ cells analyzed by mass cytometry. Each dot represents one tumor, and color indicates the PFS status at 24 months (gold: relapse and/or death, purple: absence of relapse and/or death).

Downloaded from http://aacjournals.org/cancerdiscovery/article-pdf/12/10/2280/3211219/2280.pdf by York University user on 21 January 2024

(Fig. 7C, middle) and an MHC class II-restricted release of TLS-associated CCL19 (Fig. 7C, bottom) chemokines, whereas ASC numbers increased in the coculture (Supplementary Fig. S10B). Moreover, this release was amplified by the addition of pembrolizumab (Supplementary Fig. S10B).

Next, we investigated the humoral immune responses against urinary tract and tumor commensals (Supplementary Table S7). Very high serum titers of IgG and IgA antibodies were found against commensals shared between urinary and digestive tracts (such as *E. coli* or *Enterococcus faecalis*;

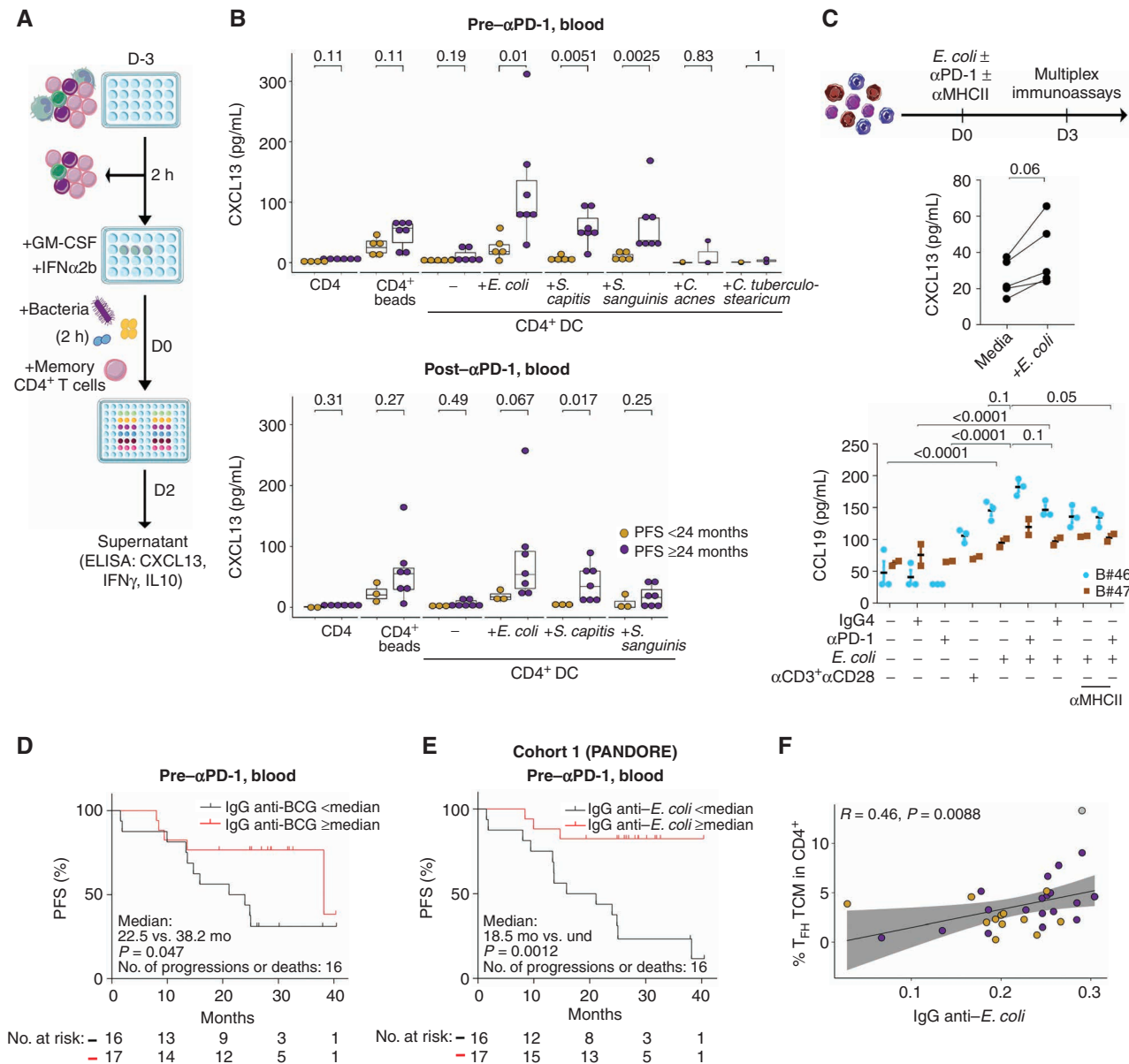


Figure 7. *E. coli*-specific humoral and cellular T $_{FH}$ memory responses are associated with PFS. **A**, Experimental setting of the CD4 $^{+}$ T-cell recall responses against bacteria (refer to Methods). **B**, Quantification of CXCL13 secretion levels in cocultures of CD4 $^{+}$ T cells isolated before treatment (top) or after treatment (bottom) and autologous monocyte-derived dendritic cells (DC) loaded with bacteria for 2 days. Patients with relapse and/or death before 24 months (gold) and without (purple) are shown. Statistical analyses used an unpaired t test (Mann-Whitney U test). *S. sanguinis*, *Streptococcus sanguinis*. **C**, Overview of the *in situ/in vitro* (*in vitro*) test with heat-killed bacteria (top). Multiplex immunoassays monitoring of CXCL13 (middle) and CCL19 (bottom) TLS-specific chemokines in *in vitro* stimulation of two to 5 freshly dissociated MIBC with *E. coli*. Different culture conditions are annotated as well as the neutralization of MHC class II complexes with specific antibodies. Medians of duplicate-triplicate wells are shown for CXCL13 (each dot corresponds to one MIBC sample) and two independent experiments performed in duplicate-triplicate wells are shown for CCL19 (each dot corresponds to one well). Statistical analyses used paired t test (middle) and two-way ANOVA (bottom). **D** and **E**, Cohort 1 (PANDORE). Kaplan-Meier curves of PFS of MIBC patients treated by pembrolizumab according to IgG against BCG (**D**; median = 0.029) and *E. coli* (**E**; median = 0.227) using titer medians as cutoff values at baseline. Statistical analysis used log-rank tests. und, undefined. **F**, Spearman correlation between TCM T $_{FH}$ cells and *E. coli*-specific IgG titers, at baseline, from PANDORE. Each dot represents one patient, and the color indicates the PFS status at 24 months (gold: relapse and/or death; purple: absence of relapse and/or death; gray: unknown). (continued on next page)

Supplementary Fig. S11F), contrasting with humoral responses toward skin commensals. Because BCG had been instilled into the bladder of 17.9% of our patients with a history of non-MIBC and given that most patients were vaccinated with BCG, we also found detectable titers of IgG against BCG that tended to decrease with neoadjuvant

pembrolizumab (Supplementary Fig. S11G). In fact, preexisting BCG-specific IgG titers were associated with PFS (Fig. 7D). In line with the clinical significance of *E. coli*-specific memory T $_{FH}$ responses, baseline *E. coli*-specific IgG (but not IgA) titers best predicted PFS in the PANDORE study (Fig. 7E; Supplementary Table S7). In addition, there was a correlation

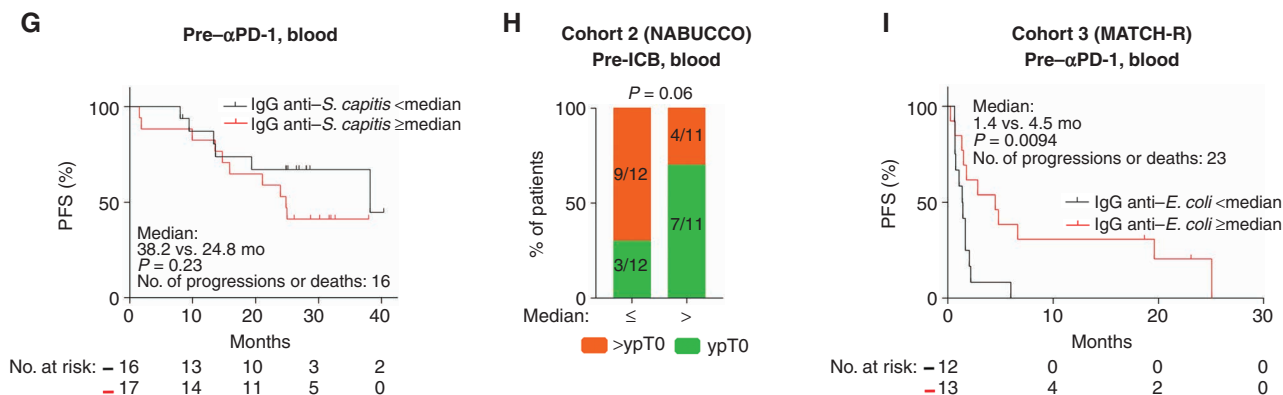


Figure 7. (Continued) G, Cohort 1 (PANDORE). Kaplan-Meier curve of PFS of MIBC patients treated by pembrolizumab according to IgG against *S. capitis* (median = 0.0024) using titer medians as cutoff values at baseline. Statistical analysis used log-rank tests. **H** and **I**, NABUCCO and MATCH-R validation cohorts. Percentages of pCR in response to neoadjuvant ipilimumab and nivolumab in patients with MIBC from the NABUCCO trial according to IgG titers against *E. coli* using titer medians as cutoff values at baseline (**H**). Kaplan-Meier curve of PFS of patients with metastatic MIBC treated with pembrolizumab according to *E. coli*-specific IgG titers using medians as cutoff values at baseline (**I**; median = 7.05). Statistical analyses used the χ^2 test (**H**) and log-rank test (**I**).

between *E. coli*-directed IgG titers and blood TCM T_{FH} cells in PANDORE (Fig. 7F). In contrast, total IgG levels or IgG specific for *S. capitis* (or other commensals) did not have any prognostic value (Fig. 7G; Supplementary Fig. S11H and S11I). In line with the frequent isolation of *S. capitis* from fresh MIBC, we found a potential clinical relevance for *S. capitis*-specific IgA responses (before and after pembrolizumab; Supplementary Table S7). Anti-*E. coli* IgG titers tended to be higher ($P = 0.06$) in patients with pCR in an independent cohort of 23 patients treated with neoadjuvant ipilimumab and nivolumab in the NABUCCO clinical trial (ref. 24; Fig. 7H), thereby supporting the findings obtained through the PANDORE cohort. Of note, Kaplan-Meier survival curves could not be designed for the NABUCCO cohort because only four events were reported at data cutoff (24). In a third independent cohort of 25 patients with metastatic MIBC treated with pembrolizumab in the MATCH-R trial (Supplementary Table S8), we again validated baseline anti-*E. coli* IgG (and not *S. capitis*-specific IgA) as a putative biomarker of PFS (Fig. 7I). We conclude that MIBC contains immunogenic *E. coli* pathogens eliciting T_{FH} and B-cell responses that predict the clinical outcome of anti-PD-1-based immunotherapy.

DISCUSSION

Here, we showed that circulating and tumor-resident T_{FH} represent prominent (albeit not exclusive) targets for neoadjuvant pembrolizumab. Such T_{FH} cells constitute a critical link with TLS where they preferentially reside and tumor infiltration by CD8 $^{+}$ T cells, culminating in clinical benefit. We used several complementary approaches (immunofluorescence, mass cytometry, functional *in vitro* assay, and flow cytometry) to show that pembrolizumab preferentially binds to effector T_{FH} , which express higher densities of PD-1 (as well as ICOS, CD40L, and Bcl6) than other TH subsets, and induces its bioactivity by promoting CXCL13 release from T_{FH} . Our dynamic study and patient longitudinal follow-up indicated that T_{FH} preexisted in the blood and tumor site prior to therapy, whereas ASCs were induced by immunotherapy and

became clinically significant only at this point. In responding patients, CXCL13-producing CD38 hi CD28 $^{+}$ CD4 $^{+}$ TILs correlated with B cells that expressed CD86 after pembrolizumab. Although baseline CD8 $^{+}$ TILs were associated with prolonged PFS, TLS-like were induced by pembrolizumab, coinciding with the local accumulation of Bcl6-expressing and CD38 $^{+}$ -activated T_{FH} .

In breast cancer, Noël and colleagues highlighted the presence of functional PD-1 hi ICOS $^{+}$ T_{FH} that provided help for the formation of active TLS, characterized by immunoglobulins, proliferating B cells, and cytotoxic CD8 $^{+}$ T-cell effectors (31). Only T_{FH} educated in active TLS had the capacity to provide T-dependent B-cell help and produce IFN γ in *ex vivo* functional assays (31). This is in line with our functional *in vitro* assay showing that preexisting T_{FH} correlated with IFN γ -producing immune-reactive bladder cancers during exposure to pembrolizumab. The functional significance of T_{FH} to instate tumor immunosurveillance has been brought up in three elegant mouse models. Hollem and colleagues dissected the orchestration of immunosurveillance in triple-negative breast cancers harboring a high mutational burden and responding to ICBs (34). The authors showed that IL21-producing T_{FH} activated B cells and stimulated the generation of class-switched plasma cells and tumor-specific IgG indispensable to control breast tumors. In line with this study, Cui and colleagues deciphered the interplay between T and B cells in a murine lung adenocarcinoma model in which tumor cells expressed neoantigens recognized by T and B cells. Cui and colleagues showed that interactions between T_{FH} and germinal center B cells promoted tumor control by CD8 $^{+}$ T cells through an IL21R-dependent pathway (64). In another preclinical model of colorectal cancer devoid of cancer antigens, bacteria-specific T_{FH} were required for the formation of TLS, bacteria-specific cytotoxic T-cell responses, and control of tumor progression (33).

In the PANDORE study, preexisting memory CXCL13-producing T_{FH} and B-cell cognate immune responses appeared to be directed against commensals common to the digestive and the urinary tracts and/or Gram $^{-}$ commensals often diagnosed

in UTIs (such as *E. coli*) in these patients. Indeed, *E. coli* IgG titers predicted long-term clinical benefit to pembrolizumab in two independent cohorts of patients. The immunostimulatory capacity of ICBs depends on the taxonomic composition of the intestinal microbiota (62, 63, 65–67). UTI are the most common bacterial infections, preferentially afflicting women, elderly persons, as well as patients with cancer (68). UTIs are typically initiated when certain gut-derived bacteria, such as UPEC, reach the bladder and invade urothelial cells. Several reports identified UPEC antigens evoking robust humoral responses that significantly reduced bladder and kidney infections upon bacterial challenge (69, 70). Cellular Th1 immune responses elicited through mucosal immunization with *E. coli* antigens were shown to be protective against bacterial rechallenge (71). Moreover, urine lymphocytes may reflect the tumor immune landscape in MIBC patients treated with ICBs and could predict recurrence-free survival (72). Although the human tumor microbiome is being deconvoluted (56, 73), new prospects for TIL generation and transfer appear to rely on exploiting MHC-restricted T-cell responses specifically directed toward intratumoral bacteria (74). Bacteria inhabiting the mucus layer close to the intestinal epithelium preferentially induce T_{FH} (75–77). Our study showed that MIBC can be invaded by a distinct commensalism comprising bacteria capable of eliciting specific T_{FH} and B-cell responses. After pembrolizumab therapy, circulating *E. coli*-specific CXCL13-producing T_{FH} tended to decrease, presumably to home to tumor lesions where they are expected to orchestrate the immune landscape of the tumor microenvironment for the long-term clinical protection against relapse. We failed to isolate UTI-related bacteria such as *E. coli* from our fresh bladder samples by culturomics and mass spectrometry but succeeded in isolating Gram⁺ bacteria (such as *S. capitis*, which was previously isolated from melanoma; ref. 74). Indeed, all patients were treated with cefazolin before radical cystectomy, likely compromising the culture isolation of live *E. coli*. Work is in progress to unveil how antigens from intraurothelial bacteria can be “cross-presented” into tumor MHC molecules to become elective targets of T_{FH} or CD8⁺ TILs. Pioneering work from Conejo-Garcia's group unraveled the biological significance of transcytosis of tumor antigen-specific and nonspecific IgA for the control of ovarian cancer (35).

These results emphasized that uropathogenic commensals, notably *E. coli* (UPEC) endowed with intrinsic immunogenicity and with tumor-invasive capacities, should be viewed as potential biomarkers of response to ICBs. In addition, UPEC may be harnessed to improve the efficacy of ICBs, for instance, by developing UPEC-based vaccines to elicit a specific T-B cross-talk prior to ICB administration. Along the same lines, extending BCG instillations beyond their current indications (for instance, including MIBC) may be instrumental prior to ICBs to boost BCG vaccine-induced immunity and offer MHC-binding targets for CD8⁺ effectors.

Regardless of these considerations, monitoring circulating T_{FH} immune responses directed against tumor or commensal antigens should be integrated in the armamentarium of biomarker discovery, in particular in the context of ICB-based therapies of tumors located at cutaneous or mucosal surfaces.

METHODS

Clinical Studies

Study Design and Population

PANDORE. PANDORE is a prospective, single-arm phase II trial testing the antitumor activity of preoperative pembrolizumab monotherapy in patients with histologically confirmed (T2–T4aN0M0) transitional cell carcinoma of the bladder (NCT03212651). Pembrolizumab was given at the recommended dose of 200 mg every 3 weeks for three cycles followed by cystectomy with appropriate lymph node dissection.

Patients were 18 years of age or older, ineligible for cisplatin or refused cisplatin-based chemotherapy, had diagnostic transurethral resection (TURBT) blocks available, and had adequate hematologic and end-organ function. Key exclusion criteria included documented severe autoimmune disease, chronic infectious disease, use of systemic immunosuppressive medications, and prior use of ICBs. Surgery was scheduled 1 to 3 weeks after the last pembrolizumab infusion. Baseline workup included thorax/abdomen/pelvis CT and standard blood analyses (hematology, biochemistry, and coagulation parameters). Neither PET-CT nor MRI was required for baseline imaging. There was no dose modification of pembrolizumab. Patients with grade 2 to 4 pembrolizumab-related toxicity (except for grade 2 infusion reaction) were required to permanently discontinue pembrolizumab administration and to proceed with radical cystectomy.

Thirteen patients (38.2%) had postoperative complications (grades 3–4) such as infection ($n = 3$), metabolism and nutrition disorders ($n = 1$), procedural complications ($n = 2$), renal and urinary disorders ($n = 4$), gastrointestinal disorders ($n = 1$), and musculoskeletal and connective tissue disorders ($n = 1$).

The trial was conducted by the French Genitourinary Group (GETUG) and funded by MSD, which provided the drug. This study was approved by the ethics committee CPP Est-III in December 2017 and the French National Agency for the Safety of Medicines and Health Products (ANSM) in November 2017, and was conducted in accordance with the protocols and Good Clinical Practice Guidelines defined by the International Conference for Harmonisation of Technical Requirements for Pharmaceuticals for Human Use and the principles of the Declaration of Helsinki.

NABUCCO (Validation Cohort). The NABUCCO study enrolled 24 patients with stage III UC treated with ipilimumab (cycle 1), ipilimumab and nivolumab (cycle 2), and nivolumab (cycle 3) followed by resection (24). A baseline serum sample was available for 23 patients who defined the validation cohort 2.

MATCH-R (Validation Cohort). MATCH-R is a prospective trial studying the evolution of the clonal architecture of tumors from patients with advanced cancer and treated with molecular targeted agents to identify mechanisms of acquired resistance (NCT02517892). The design of the study has been reported previously (78). Briefly, the primary objective of this study is to characterize molecular mechanisms of resistance to targeted therapies and immunotherapy by next-generation sequencing and the development of patient-derived xenografts and cell lines.

Patients treated with pembrolizumab with metastatic MIBC were enrolled in our study and define the validation cohort 3. Baseline, on-treatment, and postprogression biopsies were performed in patients treated with pembrolizumab. In addition, blood samples were collected longitudinally throughout the treatment and at progression in patients for collecting serum, plasma, and circulating tumor DNA.

Untreated Bladder Cancers. A cohort of 18 patients with untreated nonmetastatic MIBC was included in this study. Surgeries were performed in the University Paris-Saclay Hôpital Foch between

August 2017 and July 2021, and tumor samples were collected with appropriate written informed consent for use of clinical data and scientific purposes according to protocol reviewed and approved by the institutional ethic committee (number IRB 00012437). Before radical cystectomy, all patients were treated with cefazolin. In case of urinary tract infection, additional antibiotics have been used according to the sensitivity to other antibiotics.

Study Endpoints and Statistics

Outcomes. The primary endpoint was pCR defined as the absence of cancer cells in the bladder and the absence of microscopic lymph node metastases on the final cystectomy specimen (ypT0N0). Histopathologic examination was performed locally in each participating center by expert genitourinary pathologists on the resected primary tumor and lymph node specimens. Pathologic staging was done according to international standards and protocols. Secondary endpoints were: (i) the pathologic response (pR) defined as the absence of muscle-invasive carcinoma (≤ypT2 disease) and the absence of microscopic lymph node metastases (ypN0) on the final cystectomy specimen (defined as MPR); (ii) the number of participants with a grade 3 to 4 adverse event according to NCI Common Terminology Criteria for Adverse Events (CTCAE) version 4.0, related or not to pembrolizumab (nonrelated adverse events and immune-related adverse events were graded according to NCI CTCAE version 4.0 and reported throughout the study); and (iii) the number of patients having cystectomy. Survival outcomes were PFS defined as the time from the first dose of pembrolizumab to progression (local relapse or metastases, death, whichever occurred first) and OS defined as the time from the first dose of pembrolizumab to death, whatever the cause.

Statistical Considerations. The sample size was calculated on a precision analysis rather than a power analysis of the main outcome. The sample size was based on the CI and the CI half-width (the CI half-width is the margin of error associated with the CI). For a proportion of pCR equal to 30% and a 95% CI, 36 patients were to be included in order to obtain an estimate with certain precision of 0.15. Considering that a 10% rate of patients did not undergo cystectomy, 40 patients were needed to be recruited.

Response rates were calculated with their 95% CI by using the exact Clopper–Pearson method (based on the exact binomial distribution). PFS and OS were estimated by the Kaplan–Meier method. Median follow-up was estimated using the reverse Kaplan–Meier method. The main analysis included patients who met the eligibility criteria, had at least one cycle of pembrolizumab, and underwent cystectomy. The safety analysis included all patients who met the eligibility criteria and received at least one dose of the study drug. The clinical data cut for analysis occurred in August 2021. Data were analyzed using SAS software v-9.4 and GraphPad Prism version 7 for Windows (GraphPad Software).

Sample Collection and Processing

Sample Collection

PANDORE. Peripheral blood samples from patients enrolled in PANDORE were drawn and collected into sterile vacutainer tubes uncoated and tubes coated with heparin. Blood samples were collected at baseline (before the first cycle of pembrolizumab), right before the second and third cycles of pembrolizumab, and before and 1 month after surgery. Tumors before treatment were collected as formalin-fixed, paraffin-embedded (FFPE) tissues. Tumors after treatment were collected freshly in RPMI and as FFPE tissues. Available and analyzed samples are shown in Supplementary Fig. S5.

MATCH-R (Validation Cohort). Peripheral blood samples from patients enrolled in MATCH-R were drawn and collected into sterile vacutainer tubes uncoated for serum collection.

Untreated Bladder Cancers. Fresh tumors were collected in RPMI at +4°C.

Tissue Digestion. Tumor pieces and noninvolved bladder were collected in RPMI 1640 (GIBCO, Life Technologies, ref. 31870-025), at +4°C. The samples were stored less than 17 hours at +4°C before processing. Tissues were weighed and digested, enzymatically and mechanically. Briefly, tissues were cut into small pieces using scalpels and forceps in a petri dish. The small pieces were then dissociated in a gentleMACS Octo Dissociator (Miltenyi) using the program “37C_h_TDK_1” in a dissociation medium, which consisted of RPMI, Collagenase IV (50 IU/mL, Sigma-Aldrich; cat. #C2139), hyaluronidase (280 IU/mL, Sigma-Aldrich; cat. #H6254), and DNase I (30 IU/mL, Sigma-Aldrich, ref. 260913). Dissociation time lasted 1 hour under mechanical rotation and heating. After digestion, an aliquot of the supernatant was collected for immunoglobulin isotyping (refer to “Immunoglobulin isotyping”). The samples were then filtered through a 100-μm strainer, crushed, and washed in NaCl (Versyrene Fresenius Kabi) at 1,500 rpm for 5 minutes. The pellets were resuspended in an adapted volume of NaCl 0.9%. If required, red blood cell lysis was performed using RBC Lysis Buffer 1X (BioLegend; cat. #420301). For untreated samples, an aliquot of 50 μL was used to quantify the total number of cells and the fraction of CD45+ cells with Precision Count Beads (BioLegend; cat. #424902) by flow cytometry following the manufacturer's protocol. For PANDORE samples, the total number of cells was counted using a hemocytometer.

Serum Collection. Uncoated tubes were centrifuged for 10 minutes at 1,800 rpm. Serum was aliquoted and stored at –80°C until measurements.

Peripheral Blood Mononuclear Cell Isolation and Plasma Collection. Whole blood was layered on a Lymphocyte Separation Media (VWR; cat. #25-072-CV) in Leucosep tubes (Dutscher; cat. #227288). Tubes were centrifuged for 15 minutes at 2,000 rpm at room temperature. Plasma was collected and stored at –80°C until measurements. Peripheral blood mononuclear cells (PBMC) were collected, washed in NaCl 0.9%, and counted using a hemocytometer. Cells were washed and resuspended in fetal calf serum containing 10% of dimethyl sulfoxide (DMSO; Sigma-Aldrich; cat. #276855) for storage in liquid nitrogen.

Immunophenotyping

Mass Cytometry

Samples. For PBMCs, after thawing, cells were washed and resuspended in RPMI + 10% FCS + DNase (30 IU/mL). After 1 hour of incubation at 37°C, cells were washed and counted using Vi-Cell XR Cell Viability Analyzer (Beckman Coulter). Two million cells were used. For tumor, at least 1 million cells were used for staining by mass cytometry.

Sample Preparation. Cells were stained for viability and proliferation with rhodium (Rh103, Fluidigm; cat. #201103A; 1:100) and IdU (Fluidigm; cat. #201127; 1:2,000), respectively, in RPMI + 10% FCS for 20 minutes at +37°C. Cells were washed in staining buffer (PBS 1× + BSA 0.2% + EDTA 2 mmol/L). Cells were incubated for 5 minutes with Fc blocker (FcX, BioLegend; cat. #422302) before being stained with extracellular antibodies. For PBMCs, cells from each time point were labeled with a unique barcode by incubating with CD45-antibodies conjugated to distinct metal isotopes (Cadmium 106, 110, 111, 112, 114) before pooling. Antibodies were either purchased preconjugated from Fluidigm or purchased purified and conjugated in-house using the MaxPar X8 Antibody Labeling Kit or the MaxPar MCP9 Antibody Labeling Kit (Fluidigm) according to the manufacturer's instructions. Cells were then stained with PBMCs or a tumor panel of antibodies (Supplementary Table S1) for 30 minutes at +4°C. For PBMCs, samples were washed, fixed, and permeabilized

(Foxp3/Transcription Factor Staining Buffer Set; eBiosciences; cat. #00-55-23-00) for 40 minutes at +4°C before being stained with intracellular antibodies (Supplementary Table S1) for 30 minutes at +4°C. All samples were washed and incubated in Fix and Perm Buffer (Maxpar Fix and Perm Buffer Fluidigm; cat. #201067) for 5 minutes before being fixed in Iridium intercalator (Iridium191/193 Fluidigm; cat. #201192B; 1:4,000) diluted in PBS 1× containing 1.6% formaldehyde for 40 minutes at room temperature. Cells were washed and stored until acquisition at +4°C.

Data Acquisition. Cells were counted, washed, and resuspended in Maxpar Cell Acquisition Solution at 0.5×10^6 /mL and mixed with 10% EQ beads immediately before acquisition on a Helios mass cytometer using noise reduction, with event length limits of 10 to 150 pushes. An average of 500,000 events were acquired per sample at a flow rate of 0.03 mL/minute. Mass cytometry standard files were normalized to a global standard determined for each log of EQ beads using CyTOF Software v.6.7.1014 (Fluidigm).

Analyses. Analysis was performed with FlowJo software (Tree Star). Nonevents (doublets and debris, etc.) were removed from the analysis using the Gaussian discrimination channels (center, offset, width and residual) as recommended by Fluidigm. Circulating CD4⁺ T cells were clustered within and across samples using PhenoGraph (41). One cluster representing less than 0.075% of the total CD4⁺ T cells ($n = 854/1,159,561$ cells) was not considered in the following analysis. Clusters were then annotated manually and merged in metaclusters according to their relative expression of PD-1 (relative expression >0: PD-1⁺, relative expression = 0: PD-1⁻) and effector memory phenotype (Supplementary Table S2). Briefly, naïve, TEMRA, TE, TEM, and TCM were defined as CD45RA⁺CD28⁺CD27⁺CD127⁺, CD45RA⁺CD28⁻ and/or CD27⁻CD127^{lo}, CD45RA^{-lo}CD28^{-lo}CD27^{-lo}CD127^{-lo}, CD45RA^{-lo}CD28⁺CD27⁺CD127^{-lo}, CD45RA^{-lo}CD28⁺CD27^{+lo}CD127⁺, respectively. Then, manual gating was performed on metaclusters to define subsets (helper T cells). Tfh, Th1, Th2, Th17, and other CD4⁺ T cells were defined as CXCR5⁺CXCR3^{hi}, CXCR3⁺CXCR5⁻, CXCR3⁻CXCR5⁻CCR4⁺, CXCR3⁻CXCR5⁻CCR4⁻CCR6⁺, and CXCR3⁻CXCR5⁻CCR4⁻CCR6⁻, respectively (as illustrated in Supplementary Fig. S1A). Manual gating was performed for the analysis of B cells in PBMC samples (as illustrated in Supplementary Fig. S1B). Briefly, circulating ASCs as well as naïve, memory, nonswitched memory, and double-negative B cells were defined as CD19^{+lo}CD38^{hi}Blimp1⁺, IgD⁺CD27⁺, IgD⁻CD27⁺, IgD⁺CD27⁺, and IgD⁻CD27⁻, respectively. Manual gating was performed for tumor samples from PANDORE (as illustrated in Supplementary Fig. S3). CD4⁺ TILs and CD8⁺ TILs from untreated tumors were clustered within and across samples using PhenoGraph.

Flow Cytometry

Sample Preparation after In Sitro Tumor Assays. Cells were stained for viability with Zombie Acqua (BioLegend; cat. #423102) for 20 minutes at +4°C. Cells were washed in staining buffer and incubated during 20 minutes at room temperature with a panel of antibodies (Supplementary Table S3, panels 1 and 2) with Brilliant Strain Buffer (BD; cat. #563794). Samples were washed in staining buffer.

Sample Preparation for the Characterization of T_{FH}. Single-cell suspension of dissociated tumor tissue was centrifuged at 1,350 rpm for 5 minutes at +4°C and resuspended with FACS buffer (PBS 1×, 2% BSA, 2 mmol/L EDTA), 50 μL/staining conditions. For blocking nonspecific Fc-mediated interactions, cell suspension was incubated with 5 μL of Human TruStain FcX (Fc Receptor Blocking Solution, BioLegend; cat. #422302) at 4°C for 15 minutes. After the FcR blocking step, anti-human CXCR5 antibody was added to the FcR blocked cell suspension (2 μL/staining condition) and incubated for 20 minutes at +4°C. Combined conjugated antibodies against cell-surface

markers (Supplementary Table S3, panels 3 and 4) as well as Zombie Aqua Fixable Viability in an appropriate volume of Brilliant Violet staining buffer (BD; cat. #563794) so that the final staining volume was 100 μL (i.e., 50 μL of cell sample + 50 μL of antibody mixture) was added to the cell suspension. Stained cell suspension was incubated for 20 minutes at 4°C and washed twice with FACS buffer. For intracellular staining, after the final wash, cell suspension was fixed with 1× Foxp3 Fixation/Permeabilization working solution (eBioscience Foxp3/Transcription Factor Staining Buffer Set; cat. #00-5523-00) 35 to 40 minutes at room temperature and protected from light. Then, cell suspension was washed twice with 1× Permeabilization Buffer. The cell pellet was resuspended into 100 μL with 1× Permeabilization Buffer combining conjugated antibodies for the detection of intracellular antigens and incubated 20 minutes at 4°C, protected from light. After incubation time, stained cells were washed twice with 1× Permeabilization Buffer and the cell pellet was resuspended with FACS buffer.

Data Acquisition. Samples were acquired on a BD LSRFortessa X-20 Flow Cytometer.

Analyses. Analysis was performed with FlowJo software (Tree Star). The gating strategy is shown in Supplementary Fig. S4.

In Sitro Tumor Assays

One out of 18 samples was processed after thawing, and the others were performed freshly. Dissociated bladder cancers were stained for D0 (baseline) with mass cytometry as described in the section.

One hundred thousand CD45⁺ cells per well were incubated in complete medium [RPMI 1640 supplemented with 10% human AB serum (Institut Jacques Boy; cat. #201021334), 1% penicillin/streptomycin (GIBCO Invitrogen; cat. #15140-122), 1% L-glutamine (GIBCO Life Technologies; cat. #25030-024), and 1% sodium pyruvate (GIBCO Life Technologies; cat. #11360-039)] in a 96-well U-bottom plate. Isotype controls (IgG4 and IgG1; BioLegend; cat. #403702 and #403502, respectively; at 25 μg/mL and 5 μg/mL, respectively), recombinant IL2 (PeproTech; cat. #200-02-11, at 10 μg/mL), and anti-CD3 (Thermo Fisher Scientific, clone OKT3, at 10 μg/mL) + anti-CD28 (Thermo Fisher Scientific, clone CD28.2, at 10 μg/m) were added to control wells. AC anti-PD-1 (pembrolizumab, from Merck, at 25 μg/mL) and AC anti-CD38 (daratumumab, from Janssen-Cilag, at 5 μg/mL) were added to tested wells. Plates were incubated at +37°C with 5% CO₂ for 3 days. After incubation, cells were centrifuged at 1,500 rpm for 5 minutes. The supernatants were collected and stored at -20°C until measurements. The pellets were resuspended in PBS 1× for flow cytometry staining.

For *in vitro* assays using bacteria, cells were resuspended in an appropriate volume of TheraPEAK X-VIVO-15 Serum-free Hematopoietic Cell Medium (TheraPEAK X-VIVO-15, Lonza; cat. #BEBP02-061Q) supplemented with penicillin/streptomycin (Gibco, Invitrogen; cat. #15140-122) extemporaneously and plated at 1×10^5 CD45⁺ cells/well in a 96-well U-bottom plate. Stimulation agents [heat-killed *E. coli* Q1696 (3×10^6 /well), heat-killed *S. capitis* (3×10^6 /well), R848 (Invivogen; cat. #tlrl-r848; final concentration: 1 μg/mL) + IL2 (PeproTech; cat. #200-02-11; final concentration: 1×10^3 U/mL), and IL21 + IL4 + anti-CD40 (Human B-Poly-SE, Immunospot; cat. #CTL-hBPOLYSE-35)] were prepared extemporaneously and added to cell culture before incubation at 37°C in a humidified atmosphere of 5% CO₂ during 3 days.

Immune Response against Commensals

Bacterial Strains and Culture Conditions. Cultivable bacteria, relevant in bladder cancer patients, *E. coli* (Q1696, IHU Marseille, urine from noncancer patient), *Fusobacterium nucleatum* (P6429), *Bacteroides fragilis* (Ileon6), *E. faecalis* [Gustave Roussy (GR), urine from cancer patient], *S. capitis* (feces from kidney cancer patient nonresponder to

ICBs, EverImmune), *Staphylococcus epidermidis* (GR, urine from cancer patient), *Streptococcus mitis* (GR, urine from healthy volunteer), *Streptococcus sanguinis* (GR, urine from cancer patient), and BCG (Sanofi) were plated onto sheep's blood agar plates (COS, BioMérieux) at 37°C with 5% CO₂ in anaerobic or aerobic conditions for 48 hours and identified by Matrix Assisted Laser Desorption Ionization-Time of Flight (MALDI-TOF) mass spectrometry (Andromas; Beckman Coulter).

Assessing CD4⁺ T-cell Memory Responses. The experiments were performed as much as possible in paired settings assessing the reactivity of pre- and post-memory CD4⁺ T cells during the same experiment.

Generation of Monocyte-Derived Dendritic Cells. Frozen PBMCs were thawed, washed, and resuspended in monocyte-derived dendritic cell (mo-DC) medium (RPMI 1640 supplemented with 10% human AB, 1 mmol/L of glutamine, 1% sodium pyruvate, 1% HEPES, 1% penicillin/streptomycin). Viability and count were evaluated using a Vi-Cell XR Cell Counter. Cells were then cultured at 5 M/mL in 24-well flat-bottom plates (5M cells/well) for 2 hours at 37°C and in 5% CO₂ and separated into adherent and nonadherent cell populations. The nonadherent fraction, containing peripheral blood lymphocytes (PBL), was slowly collected, washed, and resuspended in PBL media [IMDM (Sigma-Aldrich; cat. #I3390-500 mL, supplemented with 10% human AB, 1 mmol/L glutamine, 1% sodium pyruvate, 1% HEPES, 1% penicillin/streptomycin, and 100 IU/mL rhIL2 premium grade (Miltenyi Biotec; cat. #130-097-745)]. PBLs were seeded in 24-well, round-bottom plates and cultured for 3 days at 37°C and in 5% CO₂. The adherent fraction was cultured for 67 hours at 37°C in 5% CO₂ in mo-DC differentiating medium (mo-DC media with GM-CSF (1,000 IU/mL, Miltenyi Biotec; cat. #130-093-867) and IFN α 2b (250 IU/mL, IntronA, MSD France). The volume defined to get 5 M/mL was used to resuspend PBLs and to add on the adherent fraction.

mo-DC Bacteria Cocultures. After incubation, plates containing mo-DCs were incubated for 20 minutes on ice. mo-DCs (adherent and nonadherent fraction) were harvested by flushing with cold mo-DC medium without antibiotics and washed. Cells were then counted using a hemocytometer, and the suspension was adjusted to 0.125 M/mL of mo-DC. Five thousand mo-DCs were seeded in 96-well, round-bottom plates. Bacterial suspensions containing *E. coli* (IHU Marseille, urine from noncancer patient), *S. sanguinis* (GR, urine from cancer patient), and *S. capitis* (feces from kidney cancer patient nonresponder to ICBs, EverImmune) were prepared by adjusting the turbidity at 0.3 MacFarlan in 2 mL of NaCl 0.9% (200M bacteria). The suspensions were centrifuged at 4,000 rpm for 10 minutes at +4°C and resuspended in 4 mL of mo-DC medium without antibiotics to get 50 M/mL. A multiplicity of infection of 100 was used corresponding to 500,000 bacteria per well. The plates were then centrifuged for 2 minutes at 1,000 rpm and incubated at 37°C and in 5% CO₂ for 2 hours. Wells with mo-DC alone were prepared as negative control. Wells with mo-DCs, LTA (10 ng/mL final, InvivoGen; cat. #tlrl-pstla), or LPS (10 ng/mL final, InvivoGen; cat. #tlrl-3pelp) with memory CD4⁺ T cells were also prepared as negative control. After incubation, mo-DC media with antibiotics were added to each well.

Isolation of Memory CD4⁺ T Cells and Cocultures with Bacteria. Frozen PBMCs obtained before and after pembrolizumab were thawed, washed, and resuspended in an isolation buffer (PBS 1× + 0.5% BSA + 2 mmol/L EDTA). For some experiments, PBL cultured in IL2 were pooled with fresh thawed PBMCs from the same time point. CD4⁺CD45RO⁺ T cells were isolated using the memory CD4⁺ T-cell isolating kit (Miltenyi Biotec; cat. #130-091-893) according to the manufacturer's instructions. All the steps were performed on ice. The fraction of memory CD4⁺ T cells was resuspended at

0.5 M/mL, and 100 μL was added to each well containing the mo-DC loaded with bacteria. Memory CD4⁺ T cells (without mo-DC) alone or with CD3/CD28 beads (10,000 Dynabeads per well, Dynabeads T Activator, Thermo Fisher Scientific; cat. #11131D) were used as negative and positive controls, respectively. mo-DC loaded with bacteria (without memory CD4⁺ T cells) were also cultured. The cocultures were incubated for 48 hours at 37°C in 5% CO₂. Supernatants were harvested and stored at -20°C for the determination of IFN γ , IL10, and CXCL13, as measured by commercial ELISA (details in the "Soluble factor measurements" section).

Bacterial Flow Cytometry Assay. Colonies of bacteria were picked, suspended in 1× PBS-10× glycerol at 10⁹ colony-forming units (CFU)/mL using spectrophotometer [optical density (600 nm) = 1] and frozen at -80°C. An accurate quantification of CFUs was then performed by counting bacterial events on a flow cytometer (PANDORE study: Cytoflex, Beckman Coulter; validation cohort: Canto, BD).

The IgG and IgA titers were defined with Optilite analyzer (Binding Site). All buffers were sterilized by filtration with a membrane with 0.22 μm pores. Sera were normalized at 20 μg/mL IgG or IgA in PBS 1×, 2% BSA (Sigma-Aldrich), and 0.02% sodium azide (Sigma-Aldrich). Specific serum antibody levels against purified strains were measured using a flow cytometry assay, as previously described (79). Bacterial strains (10⁶) were suspended in PBS 1×, 2% BSA, and 0.02% sodium azide in a 96-well, V-bottom plate. Twenty-five microliters of normalized sera [patients' samples or human normal immunoglobulin (IVIG, Flebogamma, Instituto Grifols) was used as a positive control or PBS as a negative control] were added to the 96-well V-bottom plate at a final concentration of 10 μg/mL, and the plates were incubated for 30 minutes at +4°C. After washing with PBS 1× (10 minutes, 4,000 g, +4°C), plates were incubated with secondary conjugated antibodies (1/400e)—either a goat anti-human IgA FITC AffiniPureGoat α chain specific or IgG Alexa Fluor 647 (or 488) AffiniPureGoat Fcγ fragment specific or isotype controls as negative controls (all from Jackson ImmunoResearch; cat. #109-095-011; cat. #709-116-073; cat. #009-090-011; and cat. #005-600-003) for 20 minutes at +4°C. Then, bacteria were washed, fixed in 25 μL paraformaldehyde (4% in PBS 1×; eBioscience) for 10 minutes at room temperature, and resuspended in sterile PBS. We used three different cytometers for three independent experiments; samples were run using a Cytoflex (Beckman Coulter for PANDORE study), another Cytoflex (Beckman Coulter for the validation cohort 2), and a Canto (BD for the validation cohort 3), and 30,000 bacterial events were acquired. Analysis was performed with FlowJo software (Tree Star). MFIs were used to measure mAb binding levels against the specific strains. For each experiment, we calculated stain index (SI) with sample MFI minus negative control MFI divided by twice the standard deviation of batch MFI (SD):

$$SI = \frac{\text{sample MFI patient} - \text{negative control MFI}}{2 \times SD}$$

For each experiment, the SD was defined using the isotype control for each plate and each strain of bacteria.

As we performed three independent experiments, MFI measurement resulted in variation due to flow cytometer variabilities. Normalization of the data was performed intraexperiment, but inter-experiment comparisons are therefore impossible.

Soluble Factor Measurements

Multiplex Immunoassays. Plasma from PANDORE was thawed at +4°C overnight and then centrifuged for 15 minutes at 1,000 × g. Plasma was monitored using a Bio-Plex Pro Human Cytokine 40-plex Assay (Bio-Rad; cat. #71AK99MR2) according to the manufacturer's instructions. Supernatants from *in vitro* assays were monitored using a Bio-Plex Pro Human Cytokine 27-plex Assay (Bio-Rad; cat.

#M500KCAF0Y) and a Bio-Plex Pro Human Cytokine 40-plex Assay (Bio-Rad; cat. #71AK99MR2; for *in vitro* stimulation with bacteria) according to the manufacturer's instructions.

Acquisitions and analyses were performed on a Bio-Plex 200 system (Bio-Rad) and using Bio-Plex Manager 6.1 Software (Bio-Rad), respectively.

ELISA. CXCL13 in the *in vitro* supernatants was detected using the Human CXCL13/BLC/BCA-1 Quantikine ELISA Kit (R&D Systems; cat. #DCX130) according to the manufacturer's instructions.

Supernatants from *in vitro* stimulations with bacteria were monitored using the Human CXCL13/BLC/BCA-1 Quantikine ELISA Kit (R&D System; cat. #DCX130), ELISA MAX Deluxe Set Human IFN γ (BioLegend; cat. #430116), and ELISA MAX Deluxe Set Human IL10 (BioLegend; cat. #430604) according to the manufacturer's instructions.

Immunoglobulin Isotyping. Supernatants collected immediately after digestion and supernatants from *in vitro* stimulations with bacteria were evaluated for immunoglobulin isotyping using the Procartaplex antibody isotyping panel 7-plex kit (Thermo Fisher Scientific, ProcartaPlex Human Antibody Isotyping Panel 7-Plex Kit; cat. #EPX070-10818-901) according to the manufacturer's recommendations. Supernatants after *in vitro* stimulations were prediluted 1:20 in fresh complete cell culture media.

Tissue Analyses

IHC, Multiplex Immunofluorescence, and PD-L1 Assessment. FFPE samples corresponding to representative slides of TURBT and cystectomies with invasive UC (IUC) were sequentially cut at 3 μ m of thickness. HES staining was performed in the first cut, so IHC and immunofluorescence stainings for CD3, CD8, CD8⁺PD-L1, CD4⁺CD38⁺PD-1, CD4⁺CD38⁺IgG4, CD20, LPS, IgG, IgA, and CD4⁺BCL6 could be performed in the subsequent ones. CD20 and IgG immunostain was performed by an anti-CD20 (DAKO; cat. #MO755, 1/100 dilution) and an anti-IgG (Abcam, #ab2410, 1/100 dilution) on a Benchmark Ultra (Roche) autostainer system. FFPE sections were deparaffinized, and subsequently antigen retrieval was conducted with CC1 buffer (pH = 8) for 36 and 64 minutes, respectively. IgA and LPS immunostaining was performed by an anti-IgA (Abcam, #ab2411, 1/200 dilution) and an anti-LPS (HycultBiotech; cat. #HM6011, 1/6,000 dilution) on a BOND-RX (Leica) autostainer system. Briefly, FFPE sections were deparaffinized, and subsequently antigen retrieval was conducted with ER1 buffer (pH = 6) for 20 and 30 minutes, respectively. Immunostained slides were revealed with the Ultraview DAB kit from Roche (CD20 and IgG) or Refine DAB from Leica (LPS and IgA). DAB chromogen was used to visualize the immunostain. Double immunostaining for CD4-BCL6 was performed by an anti-BCL6 (Dako, #M7211, 1/500 dilution) and anti-CD4 (Spring, #M3354, 1/30 dilution), in that order, on a Discovery Ultra Roche autostainer. FFPE sections were deparaffinized, and subsequently antigen retrieval was conducted with CC1 buffer (pH = 8) for 92 minutes. BCL-6 was amplified by HQ thymidine and revealed by the HQ-HRP kit, coupled to TEAL chromogen, whereas CD4 was revealed with an anti-rabbit UltraMap, coupled to DAB chromogen. A sequence of denaturation was done between the two immunostains in a CC2 buffer (pH = 6). Slides were mounted with CYTOSEAL (Fisher Scientific, #8312-4). Chromogenic slides were counterstained with hematoxylin (5–8 minutes). Triplex immunofluorescence was performed on a BOND-RX (Leica) autostainer system and an OPAL (Akoya) system. In short, FFPE sections were deparaffinized, and subsequently antigen retrieval was conducted with ER2 buffer (pH = 9) for 20 minutes. First, antibodies were added, starting with PD-1 (R&D Systems; cat. #AF1086, 1/50 dilution), CD38 (Cell Signaling Technology; cat. #51000, 1/6,000), and then CD4 (Spring; cat. #M3364, 1/400). Staining was performed using the OPAL690 polymer with OPAL520 (1/400), OPAL570 (1/1200), and OPAL690 polymer with OPAL690 (1/500), OPAL520 (1/100), and OPAL690 (1/100), respectively. Staining was performed using the OPAL690 polymer with OPAL570 (1/500), OPAL520 (1/100), and OPAL690 (1/100), respectively. Baseline PD-L1 IHC was performed by an anti-PD-L1 IHC 22C3 (Dako; cat. #M3653, 1/25 dilution) on a BOND-RX (Leica) autostainer system. In short, FFPE sections were deparaffinized, and subsequently antigen retrieval was conducted with ER2 buffer (pH = 9) for 20 minutes. An experienced pathologist (J.-Y. Scoazec) determined the CPS, and PD-L1 positivity was qualified as CPS \geq 10.

(1/50), respectively. Second, antibodies were added, starting with CD38 (Cell Signaling Technology; cat. #51000, 1/6,000), IgG4 (Epitomics; cat. #AC-0148, 1/3,000), and CD4 (Spring; cat. #M3364, 1/400). Staining was performed using the OPAL690 polymer with OPAL570 (1/500), OPAL520 (1/100), and OPAL690 (1/100), respectively. Baseline PD-L1 IHC was performed by an anti-PD-L1 IHC 22C3 (Dako; cat. #M3653, 1/25 dilution) on a BOND-RX (Leica) autostainer system. In short, FFPE sections were deparaffinized, and subsequently antigen retrieval was conducted with ER2 buffer (pH = 9) for 20 minutes. An experienced pathologist (J.-Y. Scoazec) determined the CPS, and PD-L1 positivity was qualified as CPS \geq 10.

Evaluation of TLS. Microscopic examination of HES-stained TURBT and cystectomies from patients with IUC was performed by a pathologist (L. Lordello) in order to morphologically identify TLS (LA, primary follicle-like, and secondary follicle-like). The analysis was performed in the single most representative HES slide. LA were determined as vaguely nodular aggregates of small noncleaved lymphoid cells, usually with more than 250 and fewer than 500 cells, without two or more of the early germinal center elements (follicular dendritic cells, centroblasts, mantle zone, or high endothelial veins); primary follicle-like TLS were determined as nodular aggregates of predominantly small lymphoid cells, usually with more than 500 cells, with three or more of the follicular elements, but without late germinal center elements (tinged body macrophages or dark/light areas of a clear germinal center, marginal zone); and secondary follicle-like TLS were determined as lymphoid follicles showing late germinal center structures.

Evaluation of CD20. Evaluation of CD20 was performed in a single slide in order to determine the presence of B cells in more than 50% of LA. Whole slide images (WSI) at magnifications of 20 \times and 40 \times were obtained with an Olympus scanner VS120, respectively, for HES and CD20 stainings for TURBT and cystectomies. The images were analyzed by QuPath software, version 0.2.3. TLS were annotated in WSIs in order to determine the best fit for CD20-positive dense areas (Supplementary Fig. S2). Using a simple tissue detection tool (threshold 165, requested pixel size 15, minimum area 10⁴ μ m², max fill area 10⁶ μ m², smooth image, cleanup with median filter, expand boundaries, and smooth coordinates), TLS areas were automatically annotated, whereas artifact areas were manually excluded by a pathologist (L. Lordello). The percentage of TLS area was calculated based on the whole tissue area, which had also been annotated in the WSI. Also, tumor areas were manually annotated on CD20 slides, based on HES, by a pathologist (L. Lordello).

Evaluation of CD4⁺CD38⁺PD-1⁺ and CD4⁺CD38⁺IgG4⁺ Populations in FFPE Samples. Immunofluorescence was performed for the identification of triple staining corresponding to CD4⁺CD38⁺PD-1⁺ (one slide for each TURBT and cystectomy) and CD4⁺CD38⁺IgG4⁺ (one slide for selected TURBT and each cystectomy) cells in TURBT and cystectomies. WSIs were obtained with an Olympus scanner VS120 for immunofluorescence triple staining (exposure time: 5 ms for DAPI, 30 ms FITC, and 200 ms CY3 and CY5).

Geodistribution of CD4⁺CD38⁺PD-1⁺ and CD4⁺CD38⁺IgG4⁺ in FFPE Samples. Tumor and TLS annotated areas on CD20 slides were matched to density maps generated on WSIs from triplex stainings on QuPath in order to define where CD4⁺CD38⁺PD-1⁺ and CD4⁺CD38⁺IgG4⁺ populations were located. Populations identified with the IgG4-triplex were counted within three TLS areas. L. Lordello delineated the TLS areas.

Quantification and Phenotyping of Cells. The images were analyzed by QuPath software, version 0.2.3 (80). For each panel (CD38/CD4/PD-1 and CD38/CD4/IgG4), three different classifiers, based on

fluorescence intensities, were then combined to phenotype the cells. In TLS areas, cells were detected on the DAPI channel with the cell detection tool (detection channel: DAPI, requested pixel size 0.5 μm , background radius 12 μm , median filter radius 0.5 μm , sigma 1 μm , minimum area 10 μm^2 , maximum area 400 μm^2 , threshold 80, split by shape, cell expansion 2 μm , include cell nucleus, smooth boundaries, make measurements). The resulting densities were expressed as the number of cells of each phenotype per square millimeter of tissue.

Immunoscore IC and Assessment of CD3⁺ and CD8⁺ Cells

IHC. Immunoscore IC (Veracyte) is an assay designed to measure the densities of PD-L1⁺ and CD8⁺ cells as well as the proximity between these cells on a single tissue section with image analysis tools. IHC-based staining was performed on Benchmark XT instrument (Roche-Ventana) as follows: standard deparaffinization, Cell Conditioning 1 for 54 minutes, anti-PD-L1 (clone HDX3) incubation at 37°C for 60 minutes, anti-CD8 (clone HDX1) incubation at 37°C for 60 minutes, and Hematoxylin II counterstaining for 8 minutes. Anti-PD-L1 and anti-CD8 antibodies were revealed with OptiView DAB IHC Detection Kit and ultraView Universal Alkaline Phosphatase Red Detection Kit, respectively. Immune infiltration of tumors by CD8⁺ and CD3⁺ cells was assessed on two adjacent tissue sections followed by Digital Pathology analysis with a dedicated software. Staining was adapted from Marliot and colleagues (81).

Digitization. Every stained slide was scanned with a high-resolution scanner (NanoZoomer XR, Hamamatsu) to obtain 20 \times digital images for subsequent analysis by digital pathology.

Digital Pathology. WSIs were analyzed on the HALO platform (Indica Labs) and consisted of (i) detection of the tissue section and definition of the tumor core and (ii) detection and quantification of stained cells. Subsequently, cell coordinates and phenotypes were exported to analyze their spatial distribution.

The main computed variables were CD3⁺ cell density (cells/mm²), CD8⁺ cell density, PD-L1⁺ cell density, proximity between CD8⁺ and PD-L1⁺ cells, and clustering of CD8⁺ or PD-L1⁺ cells. Arbitrarily, cutoff distances used to compute proximity and cluster indexes were set to 20 μm .

Evaluation of Bacteria in FFPE Samples

Morphologic Evaluation. Microscopic evaluation of morphologic structures that could indicate the presence of bacteria in TURBT samples was performed by a pathologist (L. Lordello). Cystic-like structures, sometimes present in cytoplasmic vacuoles filled with round or ovoid basophilic elements, were identified not only in nontumoral urothelial epithelium but also in tumor cells corresponding to IUC. These structures were quantified on the single HES slide corresponding to TURBT (33 slides). After an overview of the slide, the zone with the highest density of structures was evaluated by counting 2,000 urothelial cells, corresponding to either tumor or nontumoral urothelium, when present in the sample. Density was presented as normalized by the total number of structures/2,000 counted cells in either tumoral or nontumoral areas.

LPS Staining. IHC for LPS was performed in order to identify the occasional presence of bacteria in the samples. A group of at least five positive cells showing granular cytoplasmic staining in tumor cells corresponding to IUC was expected for the case to be considered positive. Also, normal urothelial epithelium, immune cells, and cystic-like structures were evaluated for LPS staining when present. Slides corresponding to TURBT were evaluated for LPS (33 slides).

FISH for All Bacteria, E. coli, and UPEC. FFPE deparaffinized slides corresponding to representative slides of TURBT with IUC

were sequentially cut at 3 μm of thickness. FISH was carried out as previously described (82), with the following modifications. For permeabilization of the tissues, slides were incubated for 5 minutes in a proteinase K solution (10 $\mu\text{g}/\text{mL}$) at 56°C, followed by a distilled water rinsing step. Hybridization was performed at 60°C for 3 hours using 16sRNA Eub338 (GCTGCCTCCCGTAGGAGT) for all bacteria and 5'-3' probes for uidA (F: CGCCGATGCAGATATTCTGA and R: CTGCCAGTTTCAGTTCRTTG) targeting all *E. coli*, chuA (F: GCTAC CGCGATAACTGTCTA and R: TGGAGAACCGTTCACTCTA), c3686 (F: TTGCAACAAACAGTCTACC and R: TCTGCGTCTTCTACCAT CAC), and c3509 (F: ACAATCCGCCACCATCCAG and R: CTCTC CACCGGAGAGTGT) for UPEC (60). The probes for all bacteria and all *E. coli* were coupled to Alexa 647 (Eurogentec), and the ones for UPEC were coupled to Alexa 488 fluorochrome (Eurogentec). Excess probes were removed by rinsing for 5 minutes in degrading series dilutions of saline-sodium citrate solution (4 \times , 2 \times , 1 \times , 0.5 \times , and water). Slides were then air-dried at room temperature in the dark. DAPI was used for nuclear staining. Slides were observed using the confocal microscope LSM800 with three excitation wavelengths: 595 to 600 nm for all bacteria and all *E. coli* signals, 493 nm for UPEC, and 353 nm for DAPI.

Similarly, FISH for UPEC was positive in four of the five TURBT slides tested, which were selected on the basis of positivity for LPS as well as the highest number of cytoplasmic granular structures and positive cells in different compartments (tumor, nontumor, and immune urothelial cells).

Scanning Electron Microscopy. FFPE deparaffinized slides (see "IHC, multiplex immunofluorescence, and PD-L1 assessment") were stained for 5 minutes using a 10% phosphotungstic acid solution, rinsed using distilled sterile water, and dried at room temperature. Slides were then sputtered with a 5- μm thick platinum layer using ion sputter MC1000 (Hitachi) and imaged on an SU5000 SEM (Hitachi). All acquisition settings are visible on the micrographs.

Transmission Electron Microscopy. A tissue cylinder of 2 mm was obtained from the regions of interest from FFPE blocks and processed as described (83). After rehydration, samples were kept for 4 days in glutaraldehyde 2.5% and HEPES 0.1M at 4°C. Then, samples were washed three times with PHEM 1 \times for 10 minutes. A second fixation was performed with OsO4 2% and potassium ferricyanide 1.5% in water for 2 hours. Then, samples were washed three times with water. Dehydration was performed with continuous agitation using ethanol 25%, 50%, 75%, and 95% for 15 minutes, ethanol 100% for 20 minutes, three times followed by propylene oxide for 15 minutes. Then, incubation occurred with propylene oxide/Epon A + B + DMP30 using continuous agitation overnight, and biopsies were washed three times with Epon A + B + DMP30 for 2 hours of continuous agitation. Samples were put at 60°C for 48 hours. Sections with a thickness of 70 nm were cut with a Leica UCT microtome and collected on carbon/formvar-coated copper grids. Sections were contrasted with 4% aqueous uranylacetate and Reynold's lead citrate. Stained sections were observed with a Tecnai spirit FEI operated at 120 kV. Images were acquired with an FEI Eagle digital camera. Structures corresponding to bacteria were photographed when showing membrane enhancement and core distinction from mitochondrial or lysosomal contents.

Evaluation of CD4⁺BCL6⁺ Cells. Representative cases were selected for immunostaining of CD4-BCL6 (one slide for each selected case), based on clinical and triple staining parameters (highest densities for CD4⁺CD38⁺PD-1⁺ cells). WSIs at a magnification of 20 \times were obtained with an Olympus scanner VS120 for TURBT and cystectomies. Then, images were analyzed by QuPath software, version 0.3.2. TLS were manually annotated in the WSI corresponding to TURBT or cystectomy from selected cases by a pathologist (L. Lordello). Using the cell detection tool (detection image optical density sum, requested pixel

size 1 μm , background radius 40 μm , median filter radius 0 μm , sigma 1.2 μm , minimum area 5 μm^2 , maximum area 100 μm^2 , threshold 0.1, max background intensity 2, split by shape, cell expansion 1.5 μm , include cell nucleus, smooth boundaries, make measurements), cells were automatically detected. Best thresholds for DAB (0.371, 0.553, 0.746) and blue (0.982, 0.154, 0.107) chromogens were identified based on the distribution of immunostains compared with morphology for expected CD4- and BCL6-positive areas. Sequentially, a composed classifier was created using channels for CD4 (DAB) and BCL6 (blue), regarding nucleus DAB/blue (residual) optical density mean, with thresholds of 0.15 and 0.2, respectively. The single and double positivity were calculated based on WSI or TLS annotated areas, which matched the original annotated areas on CD20 WSI.

Evaluation of IgG⁺ and IgA⁺ Cells. Representative cases were selected for immunostaining of IgG and IgA (one slide each immunoglobulin for all selected cases) based on clinical and serologic parameters. WSIs at a magnification of 20 \times were obtained with an Olympus scanner VS120 for TURBT and cystectomies. Then, images were analyzed by QuPath software, version 0.3.2. Five regions of interest measuring 1 mm^2 each, representative of similar peritumoral areas with increased immune cell infiltrate, and present in both IgG and IgA slides (sequential slides) were included for each case in paired TURBT and cystectomy. IgG- and IgA-positive cells, mostly corresponding to plasma cells, were automatically counted by QuPath fast cell counts (DAB, Gaussian sigma 1.5 μm , background radius 15 μm , use difference of Gaussians, cell detection threshold 0.1, DAB threshold 0.2) and then manually corrected by a pathologist (L. Lordello). As blood vessels were commonly stained due to the presence of free immunoglobulin, these areas, including endothelial and some perivascular cells, were not included in the counting. Then, the mean count of IgG⁺ and IgA⁺ cells was calculated considering the five regions of interest, and a ratio between IgG⁺/IgA⁺ cells was calculated. This ratio was used to evaluate changes between paired RTUV and cystectomies. TLS were manually annotated in the WSI corresponding to TURBT or cystectomy from selected cases by a pathologist (L. Lordello).

Bacteria Identification by qPCR Detection

Total genomic DNA from bladder tissues was extracted with the DNeasy Blood and Tissue Kit (Qiagen; cat. #69506) following the manufacturer's recommendation and using spin-column purification. Measurement of extracted DNA was performed using NanoDrop and normalized to 10 ng/ μL . Genomic DNA was analyzed by PowerUp SYBR Green Master Mix (Invitrogen) according to the manufacturer's instructions (2' 50°C, 10' 95°C, 45 cycles with 15" 95°C and 1' 60°C followed by 15" 95°C, 1' 60°C and 15" 95°C) using Quant Studio 3 (Applied Biosystems). Expression was normalized to the expression of the total bacterial load determined by the Universal 16S RNA gene by means of the 2^{-ΔCt} method. All primers were from Thermo Fisher Scientific. We used: ACT-CCT-ACG-GGA-GGC-AGC-AGT (all bacteria-F), ATT-ACC-GCG-GCT-GCT-GGC (all bacteria-R), CATGCCGCGTGTATGAAGAA (*E. coli*-F), and CGGG TAACGTCAATGAGCAA (*E. coli*-R).

Culturomics of MIBC

A trained pathologist (C. Radulescu) processed the tissues in sterile conditions.

The following operations were carried out in a laboratory with Biological Safety Level 2 and under a class II Microbiological Safety Station in order to avoid and limit any contamination. All materials were disinfected with 70°C alcohol.

Sample Preparation

Partitioning. When identifiable, we separated the fresh tissue into layers (muscle, fat, and mucosa) from the tumor and the non-

tumor tissues. RPMI used for the transport of the tissues was also analyzed separately.

Processing. Pestle Motor Mixer (Argos Technologies) and Homogen Sys 1.5 mL Pestle (SP Scienceware) were used to mix tissue samples.

We split each sample into 1 g of tissue per 5 mL of NaCl 0.9%.

Culture Conditions

Solid Culture Using Plates. One hundred microliters of each sample were diluted with 900 μL of NaCl; 1/10th and 1/100th dilutions were performed. A total volume of 200 μL of each dilution was used for culturing directly on 5% sheep blood-enriched Columbia Agar (COS; BioMérieux). Plates were incubated in aerobic and anaerobic atmospheres at 37°C.

Liquid Culture. Aerobic and anaerobic blood culture bottles (BD BACTEC Plus Aerobic medium; BD BACTEC Lytic Anaerobic medium) supplemented with sterile a 0.2 μm -filtered rumen (3 mL) and sheep blood defibrinated (Oxoid Limited; 3 mL) were used. Bottles were incubated at 28°C and 37°C. For each sample, 1 mL was inoculated into each of the two bottles using a syringe needle. Supplemented bottles (without samples) were used as negative controls. These vials were then processed according to the specimen to check for any contamination.

The anaerobic atmosphere was generated using an anaerobic jar (W-Zip PlasticPouches, Oxoid Limited) and an atmosphere generator (GENbox aner, BioMérieux).

Isolation and Identification

Isolation. COS plates were routinely checked, and CFUs were identified as below. For liquid cultures, on days 1, 3, 7, 10, 15, and 20, 100 μL of each sample from the BD BACTEC vials was diluted with 900 μL of NaCl 0.9%. A dilution series ranging from 1/10 to 1/100 was performed. A total volume of 200 μL of each dilution was cultured in COS plates and incubated under the same conditions as the initial bottle. Anaerobic conditions were cultivated for 5 days, whereas aerobic conditions were cultivated for 3 days. The colonies were manually subcultured onto COS plates for Matrix Assisted Laser Desorption/Ionization Time-of-Flight (MALDI-TOF) mass spectrometry (MS) identification.

Strain Identification by MALDI-TOF MS. Bacterial colonies were identified using MALDI-TOF MS (Bruker France Daltonics). Each deposit was manually performed and then covered with 2 μL of a matrix solution (HCCA-portioned-Matrix for MalDI-TOF-MS measurements in microorganism identification-(Bremen) with 500 μL of Solution OS (acetone 50%/water 47.5%/trifluoroacetic acid 2.5%; LCH CHIMIE). This analysis was performed using a MicroFlex mass spectrometer (Bruker France Daltonics) according to the manufacturer's recommendations. The acquired spectrum was then loaded into the MALDI Biotype Software (Bruker France Daltonics) and analyzed using the standard pattern-matching algorithm, which compared the spectrum acquired with that present in the library (Bruker database, constantly updated). Score values of ≥ 1.7 but < 2 indicated identification beyond the genus level, and score values of ≥ 2.0 indicated identification at the species level. Scores of < 1.7 were interpreted as not relevant. An isolate was labeled as correctly identified at the species level when at least one of the colony's spectra had a score ≥ 1.9 and one other of the colony's spectra had a score ≥ 1.7 (84).

DNA Extraction, Libraries, and Analyses from TURBT Samples

Six slides of FFPE tissues (TURBT samples) of 10 μm were used per patient.

DNA Extraction. The FFPE samples were extracted with the Maxwell Promega for the extraction of genomic DNA with the Maxwell RSC DNA FFPE Kit (Promega; cat. #AS1450) according to the manufacturer's instructions. Proteinase K treatment was done overnight at 56°C and finalized at 80°C for 4 hours. Samples were then treated with RNase before the extraction process.

Libraries. The panel targets all tumor suppressors or oncogenes covering the complete sequencing of the codifying region of a total of 411 genes and identifies point mutations, including single-nucleotide variants and small indels. The detection of copy-number variations (gains and losses of chromosomes or complete chromosomal arms) throughout the genome to specific genes and even exons was based on the coverage ratio. The total size of this panel is 1,739,310 bp. The custom panel uses the SureSelect XT HS kit (Agilent) designed for small amounts of FFPE DNA as input and detects low allelic frequencies. After the enzymatic fragmentation of 50 to 200 ng of tumoral gDNA from each sample to an average of 200 to 400 bases, the full preparation was done on Bravo equipment option B (Agilent). Library quality control was performed on Tapestation 2000 and the commercial kits D1000 reagents and D1000 ScreenTape (Agilent). DNA samples were end-repaired, dA-tailed, and ligated to the molecular-barcoded adapter system and purified using AMPure XP beads. Pooled libraries containing captured DNA fragments were subsequently sequenced on a NovaSeq 6000 platform (Illumina) as 2 × 150-bp paired-end reads. Sequences were demultiplexed using an in-house tool.

Analysis. The data analysis pipeline included the following algorithms developed internally: BWA-MEM v-0.7.12 for read alignment to the hg19 human reference genome and Samtools v-1.2 and Picard-tools v-1.139 for PCR duplicate quantification and removal. GATK Haplotype v-3.4-46, snpEff v-4.0, and Mutacaller-1.7 (home pileup internally developed) were used for variant calling and classification. Variants were called with a minimum allelic frequency threshold of 1% for already classified variants (those known in the internal database) and 5% for nonclassified variants, and a read depth threshold of 30× for the total reads at the variant location and at least 10× for the variant.

Several filters were applied to further select for potentially relevant variants among the called variants. The population databases Exac and gnomAD were used to automatically filter out polymorphism as soon as the population frequency was higher than 0.5%. Nonclassified variants (not known in the internal database) were excluded if the intrarun recurrence was superior to 4.

The tumor mutational load was assessed with the Mercury solution (Integragen) calculated by dividing the number of somatic mutations by the number of bases having a depth greater than 10. We used the data published by Lawrence and colleagues (85). The somatic mutations used for the mutational load were filtered as follows: somatic score >3, mutated allele frequency in tumor tissue ≥5%, mutated allele count in tumor tissue ≥3, population heterozygous internal database frequency ≤1%, population homozygous internal database frequency ≤1%, and EVS and 100G and Exac variant frequency ≤0.5% and consequences on protein: stop, start, missense, and splice for the SNPs and in-frame and frameshift for the indels.

Single-cell RNA-seq

Frozen samples were thawed in complete RPMI, counted, and washed in PBS 1× +0.5% BSA+2 mmol/L EDTA. The isolation and enrichment of CD45⁺ were performed using the REAlease CD45 (TIL) MicroBead Kit, human (Miltenyi Biotec; cat. #130-121-563) according to the manufacturer's instructions.

For the Rhapsody experiment, the process was done by following the manufacturer's (BD Biosciences) protocol. Two thousand four hundred and thirty-two cells were captured in a single run with seven barcoded samples pooled together. The sample was processed according to BD mRNA targeted and sample tag library preparation with

the BD Rhapsody targeted mRNA and Abseq amplification kit (Doc ID: 210969 Rev 3.0). The BD Rhapsody Immune Response Targeted Panel (Human; BD; cat. #633750) was used. Samples were then subjected to an indexed paired-end sequencing run of 2 × 151 cycles on an Illumina HiSeq 4000 system (Illumina) with 20% PhiX spike-in.

Targeted transcriptomics Fastq files were processed via the standard Rhapsody analysis pipeline (BD Biosciences) per the manufacturer's recommendations. First, R1 and R2 reads were filtered for high-quality reads, dropping reads too short (fewer than 66 bases for R1 and 64 bases for R2) or having a base quality score of less than 20. R1 reads were annotated to identify cell label sequences and unique molecular identifiers, and R2 reads were mapped to the respective reference sequences using Bowtie2. Finally, all passing R1 and R2 reads were combined and annotated to the respective molecules. For quality control of the reads, recursive substitution error correction and distribution-based error correction (DBEC) were applied, which are manufacturer-developed algorithms correcting for PCR and sequencing errors. For determining putative cells (which will contain many more reads than noise cell labels), a filtering algorithm took the number of DBEC-corrected reads into account, calculating the minimum second derivative along with the cumulative reads as the cutoff point. Finally, the expression matrix was obtained from the DBEC-adjusted molecule counts in a CSV format.

A cell was determined as a singlet if the minimum read count of a single sample tag was above the threshold of 75%. A cell was classified as a multiplet if it exceeded the threshold for more than one sample tag. A cell that did not meet the threshold was labeled undetermined. Both multiplets and undetermined cells were excluded from the analysis as described below.

For downstream analysis in Seurat V4 (Hao, Satija Cell 2020), counts were normalized, and principal component analysis (PCA) was performed. To incorporate protein information into the analysis, the Abseq signals were added to the variable genes found by the "FindVariableFeatures" function. Using these variable features and proteins, a uniform manifold approximation and projection (UMAP) was generated. Clustering was performed using shared nearest-neighbor (SNN) analysis. Differentially expressed proteins and genes were identified as FDR <0.05 and log fold change below -0.25 or above 0.25.

Analyses and General Statistical Analysis

Exploratory analyses were performed comparing PFS according to biomarker status using log-rank tests, and *P* values were not corrected for multiple testing.

Flow cytometry and mass cytometry analyses were performed with FlowJo software (Tree Star). Data representation and analyses were performed with either Prism 7 (GraphPad Software) or R v3.6 using readxl, tidyverse, dplyr, ggplot2, ggpublish, ggsignif, pheatmap, corrplot, ggdendro, Hmisc, heatmaply, and survminer packages. Heat maps of normalized marker expression (CyTOF) were generated using heatmaply R package. For *in vitro* assay, soluble factor fold ratios were calculated as log₂ transformation of median values of stimulated versus unstimulated wells and were converted to *z* scores. Heat maps were generated with the R package pheatmap. Hierarchical clustering based on the *z* score was performed using Euclidean distance and ward D2 clustering.

Data Availability

The data generated in this study are available upon request from the corresponding author.

Authors' Disclosures

C. Alves Costa Silva reports grants from MSD Avenir Foundation during the conduct of the study. C. Thibault reports personal fees and nonfinancial support from Pfizer, Merck, MSD, Janssen, and Ipsen, grants, personal fees, and nonfinancial support from AstraZeneca,

Bristol Myers Squibb, and Sanofi, and personal fees from Astellas and AAA during the conduct of the study, as well as personal fees and non-financial support from Pfizer, Merck, MSD, Janssen, and Ipsen, grants, personal fees, and nonfinancial support from AstraZeneca, Bristol Myers Squibb, and Sanofi, and personal fees from Astellas and AAA outside the submitted work. F. Audenet reports personal fees from Astellas, Urodiag, Vitadix, and Bristol Myers Squibb, and nonfinancial support from Ipsen outside the submitted work. G. Gravis reports grants from Bristol Myers Squibb, and other support from MSD, Bristol Myers Squibb, and Merck-Pfizer alliance outside the submitted work. C. Helissey reports personal fees from Janssen-Cilag, Roche, Bayer, AstraZeneca, and Astellas outside the submitted work. L. Campedel reports personal fees from MSD, Pfizer, Bristol Myers Squibb, and Bayer outside the submitted work. T. Sbarrato reports personal fees from Veracyte during the conduct of the study. T. Raoult reports grants, personal fees, and nonfinancial support from Merck Sharp & Dohme during the conduct of the study. E. Rouleau reports grants from AstraZeneca, Roche, Clovis, Bristol Myers Squibb, and MSD outside the submitted work. Y. Allory reports other support from AstraZeneca, MSD, and Bristol Myers Squibb outside the submitted work. J. Fieschi reports personal fees from Veracyte during the conduct of the study. A. Marabelle reports grants, personal fees, nonfinancial support, and other support from MSD, Bristol Myers Squibb, and AstraZeneca, and personal fees, nonfinancial support, and other support from Roche/Genentech and Pfizer outside the submitted work. J. Van Dorp reports other support from Bristol Myers Squibb during the conduct of the study. M.S. van der Heijden reports grants from Bristol Myers Squibb during the conduct of the study, as well as grants and personal fees from Bristol Myers Squibb, Roche, and AstraZeneca, grants from 4SC, and personal fees from MSD/Merck, Janssen, Pfizer, and Seagen outside the submitted work. B. Besse reports grants from 4D Pharma, AbbVie, Amgen, Aptitude Health, AstraZeneca, BeiGene, Blueprint Medicines, Boehringer Ingelheim, Celgene, Cergentis, Chugai Pharmaceutical, Cristal Therapeutics, Daiichi Sankyo, Eli Lilly, Eisai, Genzyme Corporation, GSK, Inivata, Ipsen, Janssen, Onxeo, OSE Immunotherapeutics, Pfizer, Roche/Genentech, Sanofi, Takeda, Tolero Pharmaceuticals, and Turning Point Therapeutics during the conduct of the study. F. Andre reports grants and other support from AstraZeneca and Daiichi Sankyo, grants from Lilly and Sanofi, and other support from Novartis and Relay outside the submitted work. M. Merad reports grants and personal fees from Regeneron, personal fees from Compugen, Morphic Therapeutics, Myeloid Therapeutics, Nirogy, DrenBio, Oncoresponse, Asherbio, Pionyr, Owkin, and Larkspur, other support from Innate Pharma, Genenta, DBV, and OSE Immunotherapeutics, and grants from Boehringer outside the submitted work. G. Kroemer reports grants from Daiichi Sankyo, Eleor, Kaleido, Lytix Pharma, PharmaMar, Osasuna Therapeutics, Samsara Therapeutics, Sanofi, Sotio, Tollys, Vascage, and Vasculox/Tioma, and personal fees from Reithera outside the submitted work; is on the Board of Directors for Bristol Myers Squibb Foundation France; and is a scientific cofounder of EverImmune, Osasuna Therapeutics, Samsara Therapeutics, and Therafast Bio. L. Zitvogel reports grants and personal fees from EverImmune, and grants from 9 Meters and Pileje during the conduct of the study; grants from Daiichi Sankyo outside the submitted work; and a patent for B220028EPA pending. Y. Loriot reports grants from MSD and personal fees from MSD during the conduct of the study; personal fees from Bristol Myers Squibb, Pfizer, Merck Serono, AstraZeneca, Seattle Genetics, Gilead, Taiho, and Astellas, grants and personal fees from Janssen, and grants from Roche and Celsius outside the submitted work; and a patent for EP2305181.4 pending. No disclosures were reported by the other authors.

Authors' Contributions

A.-G. Goubet: Conceptualization, formal analysis, supervision, validation, investigation, visualization, methodology, writing-original draft, project administration, writing-review and editing.

L. Lordello: Formal analysis, validation, investigation, visualization, methodology, writing-original draft, writing-review and editing. **C. Alves Costa Silva:** Investigation, visualization, methodology, writing-review and editing. **I. Peguillet:** Validation, investigation, visualization, methodology, writing-review and editing. **M. Gazzano:** Validation, investigation, visualization, methodology, writing-review and editing. **M.D. Mbognign-Fonkou:** Investigation, visualization, methodology, writing-review and editing. **C. Thelemaque:** Investigation, visualization, methodology. **C. Lebacle:** Resources, project administration. **C. Thibault:** Resources, writing-review and editing. **F. Audenet:** Resources, writing-review and editing. **G. Pignot:** Resources, writing-review and editing. **G. Gravis:** Resources, writing-review and editing. **C. Helissey:** Resources, writing-review and editing. **L. Campedel:** Resources, writing-review and editing. **M. Roupert:** Resources, writing-review and editing. **E. Xylinas:** Resources, writing-review and editing. **I. Ouzaïd:** Resources, writing-review and editing. **A. Dubuisson:** Investigation, visualization, methodology, writing-review and editing. **M. Mazzenga:** Investigation, methodology. **C. Flament:** Validation, investigation, visualization, methodology. **P. Ly:** Validation, investigation, methodology. **V. Marty:** Investigation, visualization, methodology. **N. Signolle:** Formal analysis, validation, investigation, visualization, methodology. **A. Sauvat:** Investigation, visualization, methodology. **T. Sbarrato:** Validation, investigation, visualization, methodology, writing-review and editing. **M. Filahi:** Investigation, visualization, methodology, project administration. **C. Davin:** Investigation, visualization, methodology, project administration. **G. Haddad:** Investigation, visualization, methodology. **J. Bou Khalil:** Supervision, validation, investigation, visualization, methodology. **C. Bleriot:** Supervision, validation, investigation, visualization, methodology, writing-review and editing. **F.-X. Danlos:** Investigation, visualization. **G. Dunsmore:** Formal analysis, validation, investigation, visualization, methodology. **K. Mulder:** Formal analysis, validation, investigation, visualization, methodology. **A. Silvin:** Supervision, validation, investigation, visualization, methodology, writing-review and editing. **T. Raoult:** Resources, project administration. **B. Archambaud:** Formal analysis. **S. Belhechmi:** Formal analysis, validation, writing-review and editing. **I. Gomperts Boneca:** Resources, writing-review and editing. **N. Cayet:** Investigation, visualization, methodology, writing-review and editing. **M. Moya-Nilges:** Investigation, visualization, methodology, writing-review and editing. **A. Mallet:** Resources, supervision, investigation, methodology. **R. Daillere:** Resources, writing-review and editing. **E. Rouleau:** Data curation, validation, investigation, visualization, methodology, writing-review and editing. **C. Radulescu:** Resources, project administration, writing-review and editing. **Y. Allory:** Resources, project administration, writing-review and editing. **J. Fieschi:** Supervision, validation, investigation, visualization, methodology, project administration, writing-review and editing. **M. Rouanne:** Resources, writing-review and editing. **F. Ginhoux:** Supervision, validation, writing-review and editing. **G. Le Teuff:** Conceptualization, formal analysis, supervision, validation, investigation, methodology, writing-review and editing. **L. Derosa:** Writing-review and editing. **A. Marabelle:** Conceptualization, resources, writing-review and editing. **J. Van Dorp:** Resources, writing-review and editing. **N. Van Dijk:** Resources, writing-review and editing. **M.S. van der Heijden:** Resources, writing-review and editing. **B. Besse:** Resources, writing-review and editing. **F. Andre:** Resources, writing-review and editing. **M. Merad:** Investigation, writing-review and editing. **G. Kroemer:** Writing-review and editing. **J.-Y. Scoazec:** Supervision, methodology, writing-review and editing. **L. Zitvogel:** Conceptualization, resources, formal analysis, supervision, funding acquisition, investigation, methodology, writing-original draft, project administration, writing-review and editing. **Y. Loriot:** Conceptualization, resources, supervision, funding acquisition, validation, investigation, methodology, writing-original draft, project administration, writing-review and editing.

Acknowledgments

We thank pathologists, nurses, and clinical research associates from Hôpital Européen George Pompidou, Hôpital Begin, Institut Paoli-Calmettes, Hôpital Bichat, and Hôpital Pitié-Salpêtrière for their participation in the PANDORE clinical trial. We are thankful to the flow and mass cytometry facility team of Gustave Roussy (Philippe Rameau and Cyril Catelain). We thank Fluidigm for their support. We are grateful for support for equipment from the French Government Programme Investissements d'Avenir France BioImaging (FBI; No. ANR-10-INSB-04-01) and the French Government (Agence Nationale de la Recherche) Investissement d'Avenir program, Laboratoire d'Excellence "Integrative Biology of Emerging Infectious Diseases" (ANR-10-LABX-62-IBEID). A.-G. Goubet was supported by Fondation pour la Recherche Médicale. C. Alves Costa Silva was supported by MSD Avenir. F.-X. Danlos was supported by Fondation Philantropia. M. Roupert was supported by Fondation Foch and the Association Française d'Urologie (AFU). L. Zitvogel was funded by the RHU Torino Lumière (ANR-16-RHUS-0008). L. Zitvogel and L. Derosa were supported by RHU5 "ANR-21-RHUS-0017" IMMUNOLIFE, SIRIC Stratified Oncology Cell DNA Repair and Tumor Immune Elimination (SOCRATE), as well as the SIGN'ITARC foundation. L. Zitvogel was supported by European Union's Horizon 2020 research and innovation programme under grant agreement number 825410 [project acronym: ONCOBIOME, project title: Gut OncoMicrobiome Signatures (GOMS) associated with cancer incidence, prognosis, and prediction of treatment response]. L. Zitvogel also received an ANR grant-French-German Ileobiome 19-CE15-0029-01. L. Zitvogel and G. Kroemer received a donation from the Seerave Foundation. L. Zitvogel and G. Kroemer were supported by the Ligue contre le Cancer (équipe labellisée); ANR projets blancs; Cancéropôle Ile-de-France; Fondation pour la Recherche Médicale (FRM); a donation by Elior; Institut National du Cancer (INCa); Inserm (HTE); Institut Universitaire de France; the LabEx Immuno-Oncology; and FHU CARE, Dassault, and Badinter Philantropia.

The costs of publication of this article were defrayed in part by the payment of page charges. This article must therefore be hereby marked *advertisement* in accordance with 18 U.S.C. Section 1734 solely to indicate this fact.

Note

Supplementary data for this article are available at *Cancer Discovery* Online (<http://cancerdiscovery.aacrjournals.org/>).

Received February 18, 2022; revised June 21, 2022; accepted August 2, 2022; published first August 5, 2022.

REFERENCES

- Tumeh PC, Harview CL, Yearley JH, Shintaku IP, Taylor EJM, Robert L, et al. PD-1 blockade induces responses by inhibiting adaptive immune resistance. *Nature* 2014;515:568–71.
- Ishida Y, Agata Y, Shibahara K, Honjo T. Induced expression of PD-1, a novel member of the immunoglobulin gene superfamily, upon programmed cell death. *EMBO J* 1992;11:3887–95.
- Pardoll DM. The blockade of immune checkpoints in cancer immunotherapy. *Nat Rev Cancer* 2012;12:252–64.
- Hamid O, Robert C, Daud A, Hodi FS, Hwu WJ, Kefford R, et al. Safety and tumor responses with lambrolizumab (anti-PD-1) in melanoma. *N Engl J Med* 2013;369:134–44.
- Herbst RS, Soria JC, Kowanetz M, Fine GD, Hamid O, Gordon MS, et al. Predictive correlates of response to the anti-PD-L1 antibody MPDL3280A in cancer patients. *Nature* 2014;515:563–7.
- Topalian SL, Sznol M, McDermott DF, Kluger HM, Carvajal RD, Sharfman WH, et al. Survival, durable tumor remission, and long-term safety in patients with advanced melanoma receiving nivolumab. *J Clin Oncol* 2014;32:1020–30.
- Scapin G, Yang X, Prosise WW, McCoy M, Reichert P, Johnston JM, et al. Structure of full-length human anti-PD-1 therapeutic IgG4 antibody pembrolizumab. *Nat Struct Mol Biol* 2015;22:953–8.
- Patnaik A, Kang SP, Rasco D, Papadopoulos KP, Elassais-Schaap J, Beoram M, et al. Phase I study of pembrolizumab (MK-3475; anti-PD-1 monoclonal antibody) in patients with advanced solid tumors. *Clin Cancer Res* 2015;21:4286–93.
- Wang M, Yao LC, Cheng M, Cai D, Martinek J, Pan CX, et al. Humanized mice in studying efficacy and mechanisms of PD-1-targeted cancer immunotherapy. *FASEB J* 2018;32:1537–49.
- Ribas A, Shin DS, Zaretsky J, Frederiksen J, Cornish A, Avramis E, et al. PD-1 blockade expands intratumoral memory T cells. *Cancer Immunol Res* 2016;4:194–203.
- Jordan B, Meeks JJ. T1 bladder cancer: current considerations for diagnosis and management. *Nat Rev Urol* 2019;16:23–34.
- Alfred Witjes J, Lebret T, Compérat EM, Cowan NC, De Santis M, Bruins HM, et al. Updated 2016 EAU guidelines on muscle-invasive and metastatic bladder cancer. *Eur Urol* 2017;71:462–75.
- Balar AV, Castellano D, O'Donnell PH, Grivas P, Vuky J, Powles T, et al. First-line pembrolizumab in cisplatin-ineligible patients with locally advanced and unresectable or metastatic urothelial cancer (KEYNOTE-052): a multicentre, single-arm, phase 2 study. *Lancet Oncol* 2017;18:1483–92.
- Balar AV, Galsky MD, Rosenberg JE, Powles T, Petrylak DP, Bellmunt J, et al. Atezolizumab as first-line treatment in cisplatin-ineligible patients with locally advanced and metastatic urothelial carcinoma: a single-arm, multicentre, phase 2 trial. *Lancet* 2017;389:67–76.
- Bellmunt J, de Wit R, Vaughn DJ, Frader Y, Lee JL, Fong L, et al. Pembrolizumab as second-line therapy for advanced urothelial carcinoma. *N Engl J Med* 2017;376:1015–26.
- Powles T, Durán I, van der Heijden MS, Loriot Y, Vogelzang NJ, De Giorgi U, et al. Atezolizumab versus chemotherapy in patients with platinum-treated locally advanced or metastatic urothelial carcinoma (IMvigor211): a multicentre, open-label, phase 3 randomised controlled trial. *Lancet* 2018;391:748–57.
- Powles T, Park SH, Voog E, Caserta C, Valderrama BP, Gurney H, et al. Avelumab maintenance therapy for advanced or metastatic urothelial carcinoma. *N Engl J Med* 2020;383:1218–30.
- Sharma P, Retz M, Sieffker-Radtke A, Baron A, Necchi A, Bedke J, et al. Nivolumab in metastatic urothelial carcinoma after platinum therapy (CheckMate 275): a multicentre, single-arm, phase 2 trial. *Lancet Oncol* 2017;18:312–22.
- Bajorin DF, Witjes JA, Gschwend JE, Schenker M, Valderrama BP, Tomita Y, et al. Adjuvant nivolumab versus placebo in muscle-invasive urothelial carcinoma. *N Engl J Med* 2021;384:2102–14.
- Balar AV, Kamat AM, Kulkarni GS, Uchio EM, Boormans JL, Roumiguié M, et al. Pembrolizumab monotherapy for the treatment of high-risk non-muscle-invasive bladder cancer unresponsive to BCG (KEYNOTE-057): an open-label, single-arm, multicentre, phase 2 study. *Lancet Oncol* 2021;22:919–30.
- Gao J, Navai N, Alhalabi O, Sieffker-Radtke A, Campbell MT, Tidwell RS, et al. Neoadjuvant PD-L1 plus CTLA-4 blockade in patients with cisplatin-ineligible operable high-risk urothelial carcinoma. *Nat Med* 2020;26:1845–51.
- Necchi A, Anichini A, Raggi D, Brigandt A, Massa S, Lucianò R, et al. Pembrolizumab as neoadjuvant therapy before radical cystectomy in patients with muscle-invasive urothelial bladder carcinoma (PURE-01): an open-label, single-arm, phase II study. *J Clin Oncol* 2018;36:3353–60.
- Powles T, Kockx M, Rodriguez-Vida A, Duran I, Crabb SJ, Van Der Heijden MS, et al. Clinical efficacy and biomarker analysis of neoadjuvant atezolizumab in operable urothelial carcinoma in the ABACUS trial. *Nat Med* 2019;25:1706–14.
- van Dijk N, Gil-Jimenez A, Silina K, Hendricksen K, Smit LA, de Feijter JM, et al. Preoperative ipilimumab plus nivolumab in locally advanced urothelial cancer: the NABUCCO trial. *Nat Med* 2020;26:1839–44.

25. Winoker JS, Liaw CW, Galsky MD, Wiklund P, Mehrazin R. Clinical complete response after neoadjuvant chemotherapy for muscle-invasive bladder cancer: a call for standardized assessments and definitions. *Eur Urol Focus* 2020;6:627–9.
26. Cabrita R, Lauss M, Sanna A, Donia M, Skaarup Larsen M, Mitra S, et al. Tertiary lymphoid structures improve immunotherapy and survival in melanoma. *Nature* 2020;577:561–5.
27. Helmin BA, Reddy SM, Gao J, Zhang S, Basar R, Thakur R, et al. B cells and tertiary lymphoid structures promote immunotherapy response. *Nature* 2020;577:549–55.
28. Petitprez F, de Reyniès A, Keung EZ, Chen TWW, Sun CM, Calderaro J, et al. B cells are associated with survival and immunotherapy response in sarcoma. *Nature* 2020;577:556–60.
29. Goswami S, Chen Y, Anandhan S, Szabo PM, Basu S, Blando JM, et al. ARID1A mutation plus CXCL13 expression act as combinatorial biomarkers to predict responses to immune checkpoint therapy in mUCC. *Sci Transl Med* 2020;12:eabc4220.
30. Zander R, Kasmani MY, Chen Y, Topchyan P, Shen J, Zheng S, et al. Tf^h-cell-derived interleukin 21 sustains effector CD8+ T cell responses during chronic viral infection. *Immunity* 2022;55:475–93.
31. Noël G, Langou Fontsa M, Garaud S, De Silva P, de Wind A, Van den Eynden GG, et al. Functional Th1-oriented T follicular helper cells that infiltrate human breast cancer promote effective adaptive immunity. *J Clin Invest* 2021;131:e139905.
32. Meylan M, Petitprez F, Becht E, Bougoüin A, Pupier G, Calvez A, et al. Tertiary lymphoid structures generate and propagate antitumor antibody-producing plasma cells in renal cell cancer. *Immunity* 2022;55:527–41.
33. Overacre-Delgoffe AE, Bumgarner HJ, Cillo AR, Burr AHP, Tometich JT, Bhattacharjee A, et al. Microbiota-specific T follicular helper cells drive tertiary lymphoid structures and anti-tumor immunity against colorectal cancer. *Immunity* 2021;54:2812–24.
34. Hollern DP, Xu N, Thenavan A, Glodowski C, Garcia-Recio S, Mott KR, et al. B cells and T follicular helper cells mediate response to checkpoint inhibitors in high mutation burden mouse models of breast cancer. *Cell* 2019;179:1191–206.
35. Biswas S, Mandal G, Payne KK, Anadon CM, Gatenbee CD, Chaurio RA, et al. IgA transcytosis and antigen recognition govern ovarian cancer immunity. *Nature* 2021;591:464–70.
36. Chaurio RA, Anadon CM, Lee Costich T, Payne KK, Biswas S, Harro CM, et al. TGF-β-mediated silencing of genomic organizer SATB1 promotes Tf^h cell differentiation and formation of intratumoral tertiary lymphoid structures. *Immunity* 2022;55:115–28.
37. Briganti A, Gandaglia G, Scuderi S, Gallina A, Colombo R, Fossati N, et al. Surgical safety of radical cystectomy and pelvic lymph node dissection following neoadjuvant pembrolizumab in patients with bladder cancer: prospective assessment of perioperative outcomes from the PURE-01 Trial. *Eur Urol* 2020;77:576–80.
38. Szabados B, Rodriguez-Vida A, Durán I, Crabb SJ, Van Der Heijden MS, Pous AF, et al. Toxicity and surgical complication rates of neoadjuvant atezolizumab in patients with muscle-invasive bladder cancer undergoing radical cystectomy: updated safety results from the ABCUS Trial. *Eur Urol Oncol* 2021;4:456–63.
39. Eggemont AMM, Apolone G, Baumann M, Caldas C, Celis JE, de Lorenzo F, et al. Cancer Core Europe: a translational research infrastructure for a European mission on cancer. *Mol Oncol* 2019;13:521–7.
40. Pfister C, Gravis G, Flechon A, Chevreau CM, Mahammedi H, Laguerre B, et al. 652O Dose-dense methotrexate, vinblastine, doxorubicin and cisplatin (dd-MVAC) or gemcitabine and cisplatin (GC) as perioperative chemotherapy for patients with muscle-invasive bladder cancer (MIBC): results of the GETUG/AFU VESPER V05 phase III trial. *Ann Oncol* 2021;32:S678.
41. Levine JH, Simonds EF, Bendall SC, Davis KL, Amir ED, Tadmor MD, et al. Data-driven phenotypic dissection of AML reveals progenitor-like cells that correlate with prognosis. *Cell* 2015;162:184–97.
42. Gu-Trantien C, Migliori E, Buisseret L, de Wind A, Brohee S, Garaud S, et al. CXCL13-producing TFH cells link immune suppression and adaptive memory in human breast cancer. *JCI Insight* 2017;2:91487.
43. Jones GW, Hill DG, Jones SA. Understanding immune cells in tertiary lymphoid organ development: it is all starting to come together. *Front Immunol* 2016;7:401.
44. Sautès-Fridman C, Lawand M, Giraldo NA, Kaplon H, Germain C, Fridman WH, et al. Tertiary lymphoid structures in cancers: prognostic value, regulation, and manipulation for therapeutic intervention. *Front Immunol* 2016;7:407.
45. Schalper KA, Carleton M, Zhou M, Chen T, Feng Y, Huang SP, et al. Elevated serum interleukin-8 is associated with enhanced intratumor neutrophils and reduced clinical benefit of immune-checkpoint inhibitors. *Nat Med* 2020;26:688–92.
46. Dubuisson A, Fahrner JE, Goubet AG, Terrisse S, Voisin N, Bayard C, et al. Immunodynamics of explanted human tumors for immuno-oncology. *EMBO Mol Med* 2021;13:e12850.
47. Voabil P, de Bruijn M, Roelofsen LM, Hendriks SH, Brokamp S, van den Braber M, et al. An ex vivo tumor fragment platform to dissect response to PD-1 blockade in cancer. *Nat Med* 2021;27:1250–61.
48. Huang AC, Postow MA, Orlowski RJ, Mick R, Bengsch B, Manne S, et al. T-cell invigoration to tumour burden ratio associated with anti-PD-1 response. *Nature* 2017;545:60–5.
49. Sade-Feldman M, Yizhak K, Bjørgaard SL, Ray JP, de Boer CG, Jenkins RW, et al. Defining T cell states associated with response to checkpoint immunotherapy in melanoma. *Cell* 2018;175:998–1013.e20.
50. Dubourg G, Morand A, Mekhalif F, Godefroy R, Corthier A, Yacouba A, et al. Deciphering the urinary microbiota repertoire by culturomics reveals mostly anaerobic bacteria from the gut. *Front Microbiol* 2020;11:513305.
51. Brubaker L, Wolfe A. The urinary microbiota: a paradigm shift for bladder disorders? *Curr Opin Obstet Gynecol* 2016;28:407–12.
52. Vermeulen SH, Hanum N, Grotenhuis AJ, Castaño-Vinyals G, van der Heijden AG, Aben KK, et al. Recurrent urinary tract infection and risk of bladder cancer in the Nijmegen bladder cancer study. *Br J Cancer* 2015;112:594–600.
53. Mulvey MA, Schilling JD, Hultgren SJ. Establishment of a persistent Escherichia coli reservoir during the acute phase of a bladder infection. *Infect Immun* 2001;69:4572–9.
54. Wu J, Miao Y, Abraham SN. The multiple antibacterial activities of the bladder epithelium. *Ann Transl Med* 2017;5:35.
55. Jiang X, Castelao JE, Grosheu S, Cortessis VK, Shibata D, Conti DV, et al. Urinary tract infections and reduced risk of bladder cancer in Los Angeles. *Br J Cancer* 2009;100:834–9.
56. Nejman D, Livyatan I, Fuks G, Gaverr N, Zwang Y, Geller LT, et al. The human tumor microbiome is composed of tumor type-specific intracellular bacteria. *Science* 2020;368:973–80.
57. Pushalkar S, Hundeyin M, Daley D, Zambirinis CP, Kurz E, Mishra A, et al. The pancreatic cancer microbiome promotes oncogenesis by induction of innate and adaptive immune suppression. *Cancer Discov* 2018;8:403–16.
58. Tsay JCJ, Wu BG, Sulaiman I, Gershner K, Schluger R, Li Y, et al. Lower airway dysbiosis affects lung cancer progression. *Cancer Discov* 2021;11:293–307.
59. Fu A, Yao B, Dong T, Chen Y, Yao J, Liu Y, et al. Tumor-resident intracellular microbiota promotes metastatic colonization in breast cancer. *Cell* 2022;185:1356–72.
60. Brons JK, Vink SN, de Vos MGJ, Reuter S, Dobrindt U, van Elsas JD. Fast identification of Escherichia coli in urinary tract infections using a virulence gene based PCR approach in a novel thermal cycler. *J Microbiol Methods* 2020;169:105799.
61. Daillère R, Vétizou M, Waldschmidt N, Yamazaki T, Isnard C, Poirier-Colame V, et al. Enterococcus hirae and barnesiella intestini-hominis facilitate cyclophosphamide-induced therapeutic immunomodulatory effects. *Immunity* 2016;45:931–43.
62. Routy B, Le Chatelier E, Derosa L, Duong CPM, Alou MT, Daillère R, et al. Gut microbiome influences efficacy of PD-1-based immunotherapy against epithelial tumors. *Science* 2018;359:91–7.
63. Vétizou M, Pitt JM, Daillère R, Lepage P, Waldschmidt N, Flament C, et al. Anticancer immunotherapy by CTLA-4 blockade relies on the gut microbiota. *Science* 2015;350:1079–84.

64. Cui C, Wang J, Fagerberg E, Chen P-M, Connolly KA, Damo M, et al. Neoantigen-driven B cell and CD4 T follicular helper cell collaboration promotes anti-tumor CD8 T cell responses. *Cell* 2021;184:6101–18.
65. Gopalakrishnan V, Spencer CN, Nezi L, Reuben A, Andrews MC, Karpinets TV, et al. Gut microbiome modulates response to anti-PD-1 immunotherapy in melanoma patients. *Science* 2018;359:97–103.
66. Matson V, Fessler J, Bao R, Chongsuwat T, Zha Y, Alegre ML, et al. The commensal microbiome is associated with anti-PD-1 efficacy in metastatic melanoma patients. *Science* 2018;359:104–8.
67. Sivan A, Corrales L, Hubert N, Williams JB, Aquino-Michaels K, Earley ZM, et al. Commensal *Bifidobacterium* promotes antitumor immunity and facilitates anti-PD-L1 efficacy. *Science* 2015;350:1084–9.
68. Flores-Mireles AL, Walker JN, Caparon M, Hultgren SJ. Urinary tract infections: epidemiology, mechanisms of infection and treatment options. *Nat Rev Microbiol* 2015;13:269–84.
69. Abraham SN, Sun D, Dale JB, Beachey EH. Conservation of the D-mannose-adhesion protein among type 1 fimbriated members of the family Enterobacteriaceae. *Nature* 1988;336:682–4.
70. Asadi Karam MR, Oloomi M, Mahdavi M, Habibi M, Bouzari S. Vaccination with recombinant FimH fused with flagellin enhances cellular and humoral immunity against urinary tract infection in mice. *Vaccine* 2013;31:1210–6.
71. Wu J, Bao C, Reinhardt RL, Abraham SN. Local induction of bladder Th1 responses to combat urinary tract infections. *Proc Natl Acad Sci U S A* 2021;118:e2026461118.
72. Wong YNS, Joshi K, Khetrapal P, Ismail M, Reading JL, Sunderland MW, et al. Urine-derived lymphocytes as a non-invasive measure of the bladder tumor immune microenvironment. *J Exp Med* 2018;215:2748–59.
73. Sepich-Poore GD, Zitvogel L, Straussman R, Hasty J, Wargo JA, Knight R. The microbiome and human cancer. *Science* 2021;371:eabc4552.
74. Kalaora S, Nagler A, Nejman D, Alon M, Barbulin C, Barnea E, et al. Identification of bacteria-derived HLA-bound peptides in melanoma. *Nature* 2021;592:138–43.
75. Ansaldi E, Slayden LC, Ching KL, Koch MA, Wolf NK, Plichta DR, et al. Akkermansia muciniphila induces intestinal adaptive immune responses during homeostasis. *Science* 2019;364:1179–84.
76. Roberti MP, Yonekura S, Duong CPM, Picard M, Ferrere G, Tidjani Alou M, et al. Chemotherapy-induced ileal crypt apoptosis and the ileal microbiome shape immunosurveillance and prognosis of proximal colon cancer. *Nat Med* 2020;26:919–31.
77. Xu M, Pokrovskii M, Ding Y, Yi R, Au C, Harrison OJ, et al. c-MAF-dependent regulatory T cells mediate immunological tolerance to a gut pathobiont. *Nature* 2018;554:373–7.
78. Recondo G, Mahjoubi L, Maillard A, Loriot Y, Bigot L, Facchinetto F, et al. Feasibility and first reports of the MATCH-R repeated biopsy trial at Gustave Roussy. *NPJ Precis Oncol* 2020;4:27.
79. Moor K, Fadlallah J, Toska A, Sterlin D, Balmer ML, Macpherson AJ, et al. Analysis of bacterial-surface-specific antibodies in body fluids using bacterial flow cytometry. *Nat Protoc* 2016;11:1531–53.
80. Bankhead P, Loughrey MB, Fernández JA, Dombrowski Y, McArt DG, Dunne PD, et al. QuPath: open source software for digital pathology image analysis. *Sci Rep* 2017;7:16878.
81. Marliot F, Chen X, Kirilovsky A, Sbarrato T, El Sissy C, Batista L, et al. Analytical validation of the Immunoscore and its associated prognostic value in patients with colon cancer. *J Immunother Cancer* 2020;8:e000272.
82. Grine G, Terrer E, Boualam MA, Aboudharam G, Chaudet H, Ruimy R, et al. Tobacco-smoking-related prevalence of methanogens in the oral fluid microbiota. *Sci Rep* 2018;8:9197.
83. Graham L, Orenstein JM. Processing tissue and cells for transmission electron microscopy in diagnostic pathology and research. *Nat Protoc* 2007;2:2439–50.
84. Seng P, Drancourt M, Gouriet F, La Scola B, Fournier P-E, Rolain JM, et al. Ongoing revolution in bacteriology: routine identification of bacteria by matrix-assisted laser desorption ionization time-of-flight mass spectrometry. *Clin Infect Dis* 2009;49:543–51.
85. Lawrence MS, Stojanov P, Polak P, Kryukov GV, Cibulskis K, Sivachenko A, et al. Mutational heterogeneity in cancer and the search for new cancer-associated genes. *Nature* 2013;499:214–8.